ACTIVE DAMPING OF A STRUCTURE WITH LOW-FREQUENCY AND CLOSELY-SPACED MODES: EXPERIMENTS AND THEORY

by

George C. Schamel II

Thesis submitted to the Faculty of the

Virginia Polytechnic Institute and State University

in partial fulfillment of the requirements for the degree of

MASTER OF SCIENCE

in

Aerospace Engineering

APPROVED:

William L. Hallauer, Jr.

Raphael T. Haftka

Frederick H. Lutze

March, 1985
Blacksburg, Virginia

ACTIVE DAMPING OF A STRUCTURE WITH LOW-FREQUENCY AND CLOSELY-SPACED MODES: EXPERIMENTS AND THEORY

by

George C. Schamel II

ABSTRACT

This thesis covers the investigation of active damping on a cruciform beam laboratory structure along with the development of this structure. Also important to this and other research was the development of a calibration apparatus that produces accurate, repeatable calibrations for several types of laboratory instruments. The cruciform beam model is developed out of a simpler beam-cable model with the addition of a crosspiece that produces a pair of closely-spaced modes. This model is developed theoretically and verified experimentally. Experimental verification is also obtained for theoretical results in the simultaneous design of a structure and control system. A spatial filtering method for determining the modal response of the structure from the physical response is also investigated.

ACKNOWLEDGEMENTS

I am greatly indebted to Dr. William L. Hallauer Jr., my advisor, for his guidance and patient assistance throughout the course of this research. The original concept for this study was his and his constant availability and insight helped solve many problems encountered in this research.

I also thank Dr. Raphael Haftka and Dr. Fred Lutze for serving on my graduate committee.

This research has been supported by NASA Langley Research Center under NASA Grant NAG-1-224 and by the Air Force Office of Scientific Research under AFOSR Contract F49620-83-C-0158.

I extend my gratitude to the National Science Foundation for NSF Grant number CME-8014059, which purchased the data acquisition equipment used in the experimental part of this research.

Thanks are due to Mr. Gary Skidmore and Mr. Russ Gehling for their able assistance during this research.

I am indebted to Mr. Gary Stafford for his technical support in the laboratory. I am also indebted to Mr. Jake Frazier, Mr. Frank Shelor, and Mr. Kent Morris for their work on the fabrication of equipment used in this research.

My deepest gratitude goes to my Sensei, Mr. Ed L. Hampton, for without his training I never would have completed this thesis.

TABLE OF CONTENTS

Appendix

LIST OF TABLES

LIST OF FIGURES

Figure

page

Chapter I

INTRODUCTION

Active vibration control of large space structures (LSS) has been a subject of great interest in recent years as more such structures are being studied. Although the purposes of these LSS may greatly vary, they will probably have certain common characteristics. In particular, high modal density at low frequencies, closely-spaced modes, and low inherent damping are important pathologies. The theoretical and experimental studies of active vibration control are primarily directed at substantially increasing the damping. In addition to designing the control system, some studies have been conducted in the simultaneous design of the control system and the structure.

Some previous studies (Refs. 1, 2, and 3) have used the same structure and control hardware considered here to study different types of theoretical control strategies. In particular, Ref. 1 looked at applying direct velocity feedback to the same basic structure used for the work in this thesis. The basic structure used in Refs. 1, 2, and 3 was an 80 x 2 x 1/8 inch steel beam suspended between ceiling and floor with cables in tension (Figure 1). This structure was designed to have five structural modes of vibration below 30 Hz and very low inherent damping.

One purpose of this research was to develop from this basic laboratory structure a modified structure whose natural modes of vibration not only had low frequencies but also contained two modes closely spaced in frequency. Once this structure was developed both theoretically and experimentally with good agreement in frequencies and mode shapes, various theoretical designs for active damping (control) systems were to be verified experimentally.

This thesis covers many aspects of the experimental side of this research along with some theoretical developments. Chapter II describes the development of an essential calibration device for the control sensors and actuators used. Chapters III and IV cover the development of a theoretical model and the subsequent experimental verification of that model. The experimental validation of active damping designs coupled with favorable minor structural modifications is covered in Chapter V. Chapter VI describes the development and testing of a modal filter based on the structural mode shapes. Chapter VII contains a summary of the major accomplishments described in the previous chapters.

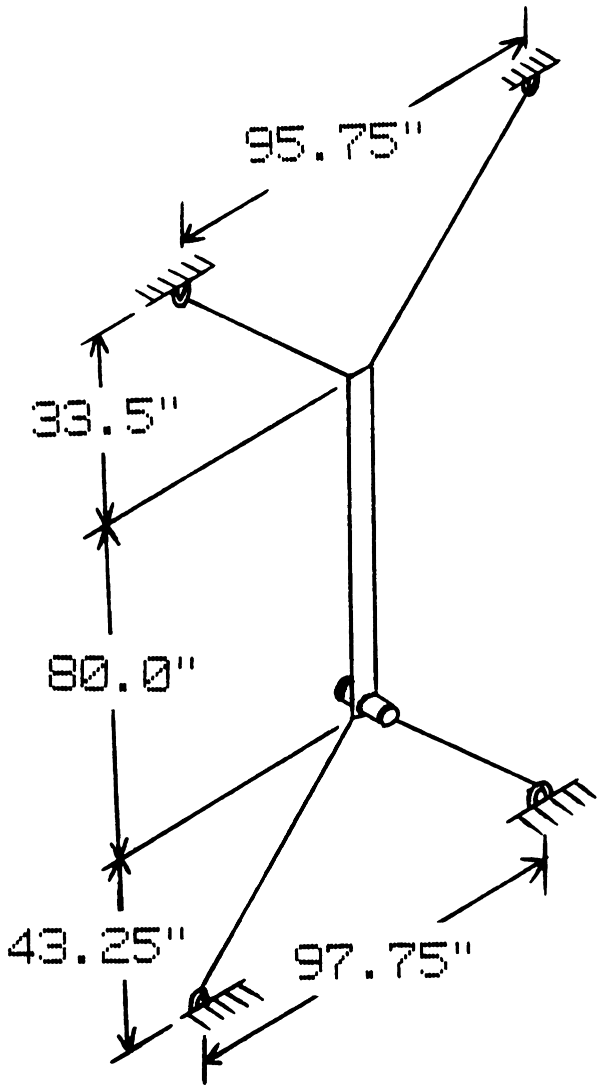

Figure 1: Line drawing of beam-cable experimental structure.

Chapter II

CALIBRATION APPARATUS

The experimental work described in this thesis and in Refs. 1-4 have all required the use of non-contacting velocity sensors and force actuators. These velocity sensors and force actuators consist of magnetic field structures which have no contact with the structure and small coils which are mounted on the structure, (Figure 2). There are three types of field structures presently in use. The first type, based on a dismantled vibration exciter, is described in Reference 1. The second type, based on a large ring magnet, is described in Reference 4. The third design was developed for the work reported here and is described in detail in Appendix A. The coils vibrate in the radial magnetic field generated by the magnetic field structures. According to electromagnetic field theory, the voltage generated by the motion of a wire in a magnetic field is directly proportional to the velocity at which it is moving. Furthermore, a current imposed on a coil in a magnetic field produces a force proportional to the current. These field structure-coil pairs are excellent laboratory instruments for the excitation, control, and observation of an experimental model. A major problem with these magnetic field structure-coil pairs is the difficulty in obtaining an accurate calibration factor either in volts/velocity or force/ampere. For Refs. 1-6 velocity sensors were calibrated in place on the structure. This procedure caused complications and inaccuracies in the calibration factors due to the interactions with the dynamics of the structure. The calibration of the force actuators for Refs. 1-6 was performed separately from the laboratory structure but required the accurate positioning of a very heavy object to provide a hard point for the actuator to push against. During this process, there was a risk of damaging the coil. Due to these problems and the large number of these magnetic field structure-coil pairs used in the experimental research, the need for a better method of calibration became apparent.

2.1 DESIGN OF THE APPARATUS

The main requirements for the calibration apparatus were the following. First, the design was to remain simple so that it would be relatively quick and easy to calibrate a number of sensors or actuators in a short period of time. Second, the main framework of the apparatus had to be stiff enough to be effectively rigid during the tests. Third, the dynamics of the flexible part of the apparatus where the coil would be mounted should have minimal effect on the calibration procedure. The fourth and last requirement put on the design was flexibility of use, i.e. the apparatus should be useful in the calibration of a number of laboratory instruments.

Figure 3 is an oblique line drawing of the final design of the calibration apparatus. The basic structure of the apparatus is a 6 x 12 x 24 inch frame with the 12 x 24 inch sides open. Aluminum plates of 3/4 in. thickness were used for the sides to provide adequate rigidity. The plates were fastened together with three countersunk screws at each joint to provide relatively rigid corners. Support blocks were put under the base so that clamps could be used to hold either shakers or field structures to the bottom of the frame. To prevent any movement of the base of the frame when a shaker was in use, a central support was attached providing a rigid point for the shaker to push against. The central beam on the apparatus, where the instruments to be calibrated are attached, is supported from either side of the box by clamps made from half-inch angle iron. Two slots were cut in the sides of the box so that the angle iron clamps and therefore the central beam could be moved up and down for exact positioning. Horizontal positioning of the beam was allowed for in the design of the angle iron clamps.

The bottom iron has two threaded holes in it and the top iron has two unthreaded holes. This allows the central beam to be moved front to back and side to side between the bolts before the bolts are tightened. When tightened, the angle iron clamps provided good clamping on both ends of the central beam. Two different central beams were used for different calibrations. A flexible aluminum beam 1.5 inches wide by 1/8 inch thick was used for the calibration of the velocity sensors and the proximity probes. A very stiff aluminum beam 1 inch wide by 1/2 inch thick was used for the calibration of the force actuators.

2.2 CALIBRATION PROCEDURES

The primary use of this calibration apparatus is the calibration of magnetic field structure-coil pairs. In general, to do this calibration, the coil must be moved within the magnetic field and the voltage output across or the current through the coil must be related to some calibration standard. Two types of calibrations were needed for the magnetic field structure-coil pairs, a velocity sensor calibration and a force actuator calibration. Also, the apparatus was used to calibrate Bently-Nevada proximity probes (see Ref. 5 for detailed description of the probes). Each type of calibration will be described separately in this section.

The calibration standard used for all of the velocity calibrations was a PCB Piezoelectric Low-Frequency Accelerometer model 308B09. The acceleration is measured directly opposite the velocity coil and then integrated so that both signals represent the velocity at that point. A Fast Fourier Transform (FFT) is then applied to both signals. The voltage FFT from the velocity coil is then divided by the integrated (in the frequency domain) acceleration FFT yielding the calibration of that velocity coil in units of volts per velocity unit.

The setup procedure was relatively simple, but as usual several pitfalls were discovered in the first few uses of the apparatus. In the setup procedure, the heavier pieces of equipment were placed first so that most of the positioning adjustment could be done with the lighter items. The very first piece set up is the magnetic field structure. It is roughly positioned on the inside top of the apparatus. Two clamps are used to secure the wooden base of the magnetic field structure in position. Next, small plexiglas mounts for the accelerometer and the sting attachment for the shaker are mounted with glue near the center of the flexible beam. These plexiglas mounts are 1/2 inch square by 1/8 inch thick with a small, threaded hole in the center for the mounting studs. The velocity coil is glued directly opposite the mount for the accelerometer. Any common brand of "super" glue proved sufficient for these attachments. Figure 4 is a photograph of the calibration apparatus completely set up for the calibration of a velocity sensor. The magnetic field structure-coil pair can be clearly seen mounted opposite the PCB accelerometer. Figure 5 is a close-up photograph of the magnetic field structure-coil pair and the accelerometer. In front of the accelerometer, the sting attachment for the shaker can be seen.

For a good dynamic calibration, the center of the accelerometer mount must be aligned with the axis of the velocity coil. Otherwise, the calibration curve will show signs of a resonance in the 40-50 Hz range. This resonance can reduce the accuracy of the calibration. The resonance is a torsional mode of the flexible beam combined with the mounted instrumentation. Now that the coil and accelerometer mount are properly aligned, the beam should be placed in the angle iron clamps but not yet clamped. The flexible beam and angle iron clamps may now be raised until the coil is nearly touching the magnetic field structure. Adjust the beam in the horizontal plane so that the coil will be properly aligned with the gap in the magnetic field structure. The angle iron clamps must then be raised enough so that 3/8 inch of the coil (level previously marked with tape) is inside the magnetic field structure. Carefully tighten the screws on the angle iron clamps on alternate sides such that no bending is induced in the flexible beam. Now the shaker is set under the center of the flexible beam so that it pushes against the center support of the calibration apparatus. Clamp the shaker in position and choose the proper length sting to attach the shaker to the plexiglas mount on the flexible beam. Again, no bending should be present in the beam at this point. Only one last item remains to be mounted, the PCB Low Frequency Accelerometer. It must be secured to the plexiglas mounting block using a small set screw. The set screw attaches the base of the accelerometer to the mounting block.

Once the apparatus is set up, the calibration may proceed. The voltage from the sensing coil is put into one channel of the data acquisition and analysis system and the acceleration signal in another channel. The data acquisition and analysis system (DAAS) is a microcomputer based system developed by Synergistic Technology Inc. (STI), of Cupertino, California. The system consists of multi-channel data acquisition and signal generation hardware teamed with a computer, two disk drives, and a display terminal. The system uses the Vibration Analysis and Measurement Processor (VAMP Version 5A), also from STI. The

DAAS generates the excitation signal with which the system is excited. For these tests, the excitation signal used was a windowed sine chirp. The sine chirp starts at very low frequency and increases in frequency linearly in time to 40 Hz. A windowed sine chirp used was a sine chirp which had been multiplied by a function with a unit value out to 30 Hz, linearly decreasing to zero at 35 Hz, and zero to 40 Hz. Both the acceleration and velocity signals are multiplied by a preset input gain so that the computer has enough voltage amplitude to work with. Common input gains range between 11 and 101 depending on the peak voltage expected. Once both the time series signals have been Fast Fourier Transformed they are divided by the input gain within the VAMP software. It is here that the acceleration signal is multiplied by its calibration factor and then integrated to get the velocity. The velocity signal in volts is now divided by the integrated acceleration signal to produce the dynamic calibration curve of the velocity coil. This curve is commonly smoothed to remove the effects of noise in the signals. The smoothing function in the VAMP software takes the data point in question and averages N values before and after the center point. The smoothing command is SM#, where the # is equal to 2N+1. Figure 6 is sample calibration curve of one of the velocity sensors. The frequency resolution was 0.0781 Hz for all calibrations. The calibration curve drops off at the lower frequencies because the accelerometer signal is not good at the lower frequencies. The curve is not good above 30 Hz as well because the anti-aliasing filters in the DAAS roll off at 30 Hz.

The setup of the calibration apparatus for the calibration of a Bently-Nevada proximity probe is much the same as the setup for the calibration of a velocity sensor. The shaker and accelerometer attachments are set up the same with the minor exception of a 2 x 1/8 inch steel bar clamped between the shaker and the bottom of the calibration apparatus to provide a mount for the dial gauge holder holding the proximity probe. A magnetic clamp holds the dial gauge holder to the steel bar and the arm arrangement allows for the positioning of the proximity probe. The proximity probe is positioned directly opposite the accelerometer to avoid any inaccuracies. Follow the same data acquisition procedure as with the velocity sensor but integrate the acceleration twice to obtain the displacement. Figure 7 is a photograph of the calibration apparatus set up to calibrate a proximity probe.

The setup for the calibration of a coil-magnetic field structure force actuator is completely different from the previous two setups. The flexible beam is replaced with a much thicker beam which can be considered rigid for these purposes. A PCB model 208B force gauge powered by a PCB model 480B power unit is attached to the bottom center of the rigid beam using a plexiglas mounting block, and the coil to be calibrated is attached to the other side of the force gauge. The magnetic field structure is clamped to the bottom center of the calibration apparatus. Then the rigid beam is put in the angle iron clamps and lowered to the field structure. The coil is centered and lowered 3/8 inch past the top of the field structure into the gap. A force is generated by passing a current through the coil in the magnetic field. The DAAS generates an excitation voltage, and a current controlled power amplifier (Ref. 3) is used to produce a current directly proportional to voltage. The voltage put into the power amplifier is acquired by the DAAS and multiplied by a calibration constant that relates the voltage into the power amplifier to the force out of the force actuator. A transduction constant of .25 amperes/volt is applied by the power amplifier. Therefore, the voltage signal acquired by the computer is multiplied by 0.25 so that it represents the current in the coil. The signal from the force gauge is multiplied by its calibration constant. Its FFT is then divided by the FFT of the signal put into the force coil, resulting in a calibration curve in force/ampere versus frequency. Figure 8 is a photograph of the calibration apparatus set up for the calibration of a force actuator. Note the force gauge located between the coil and the rigid beam.

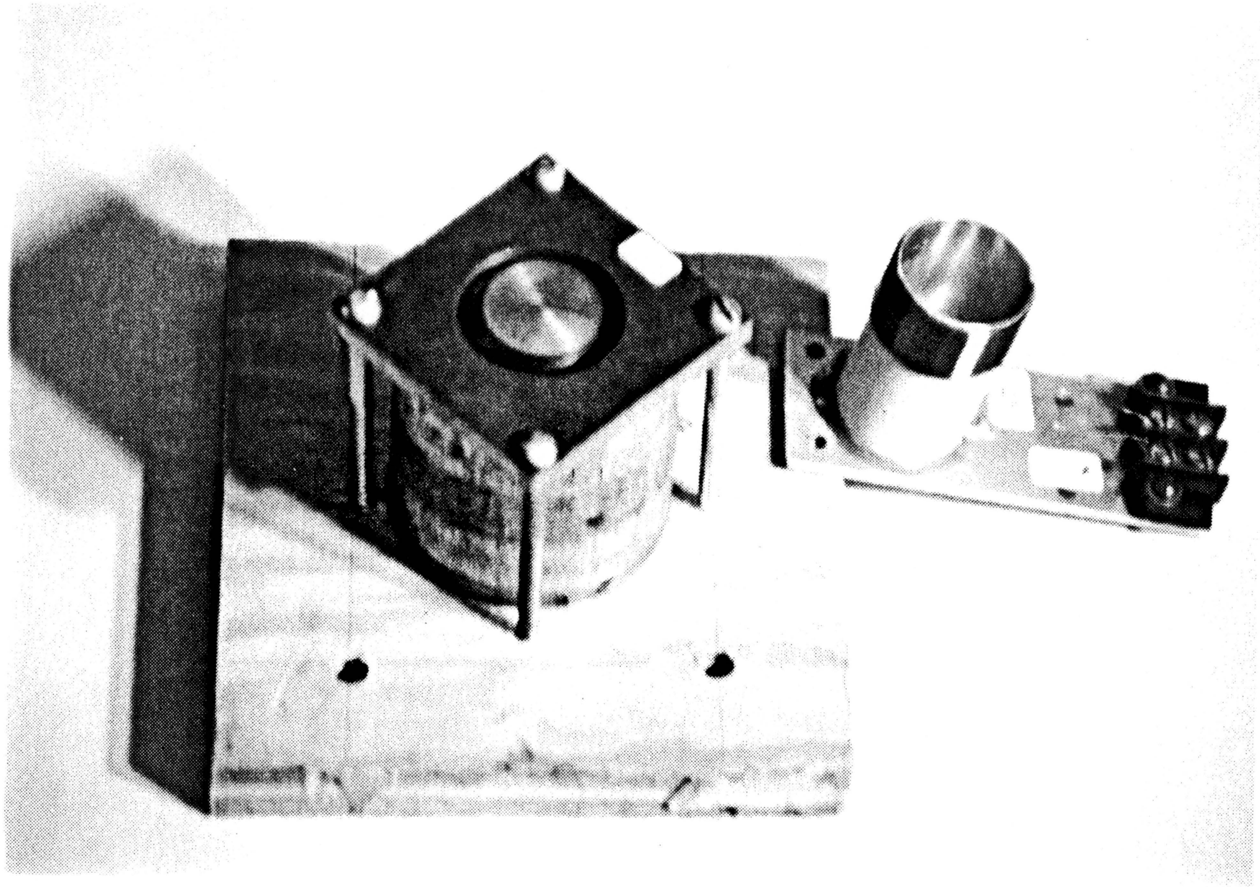

Figure 2: Photograph of a magnetic field structure and sensing coil.

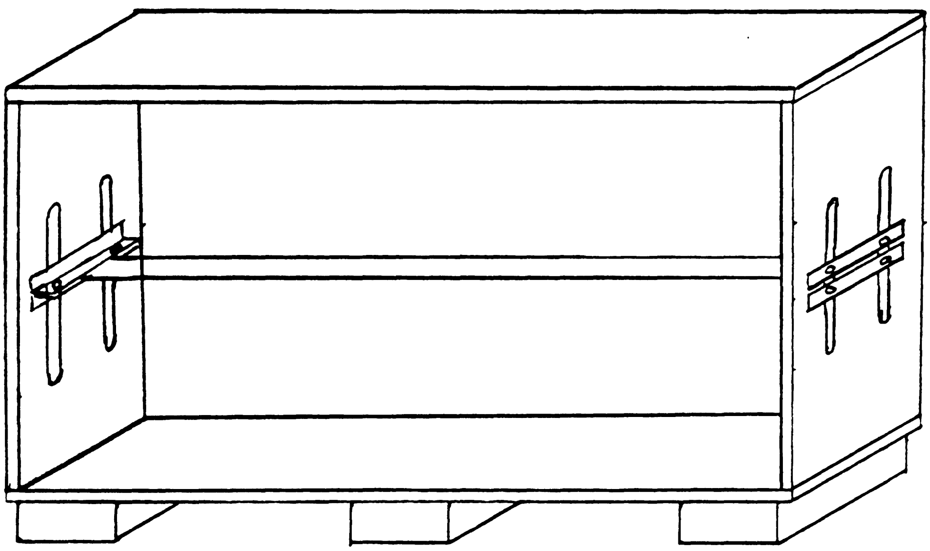

Figure 3: Line drawing of the calibration apparatus.

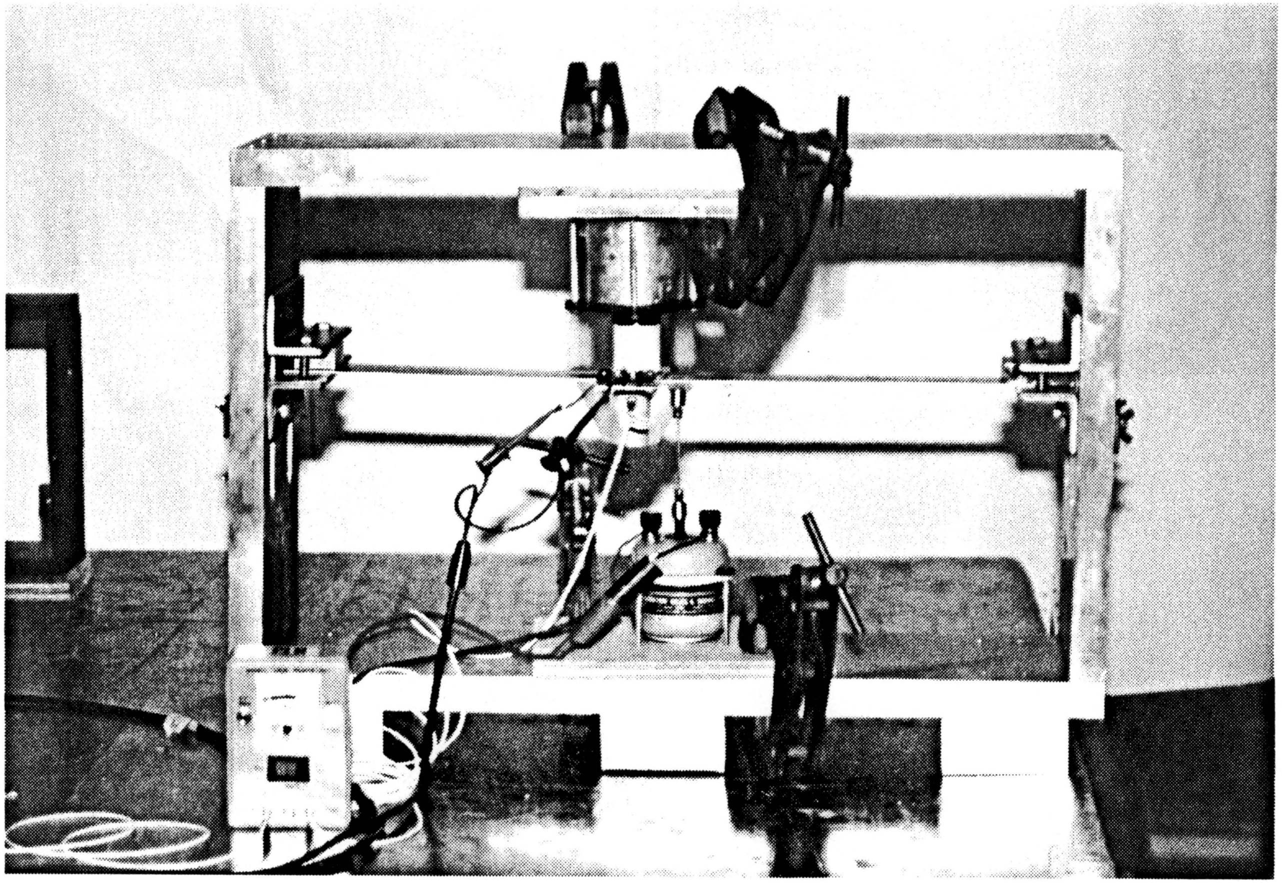

Figure 4: Photograph of the calibration apparatus set up for the velocity calibration of a magnetic field structure-coil pair.

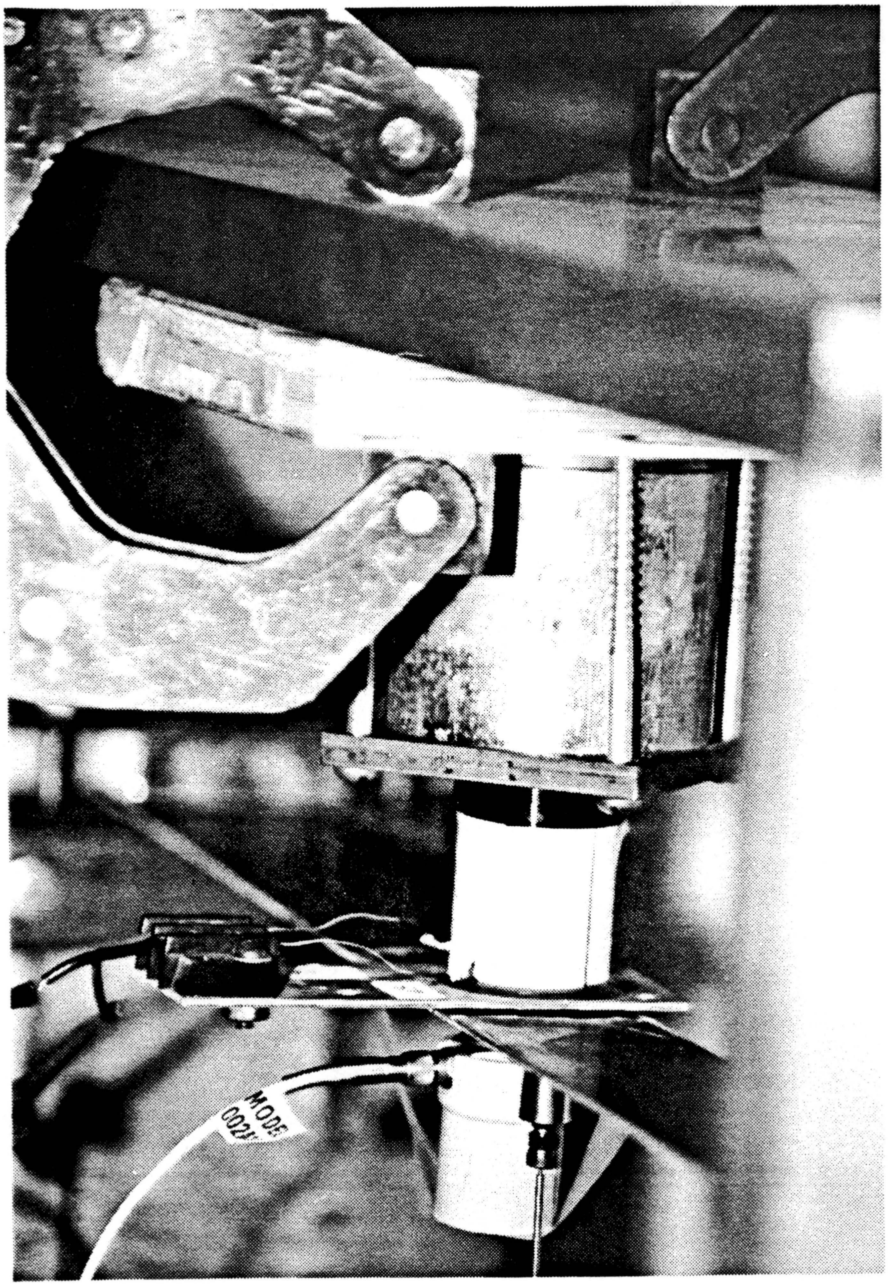

Figure 5: Close-up photograph of the velocity sensing coil and the accelerometer in proper alignment.

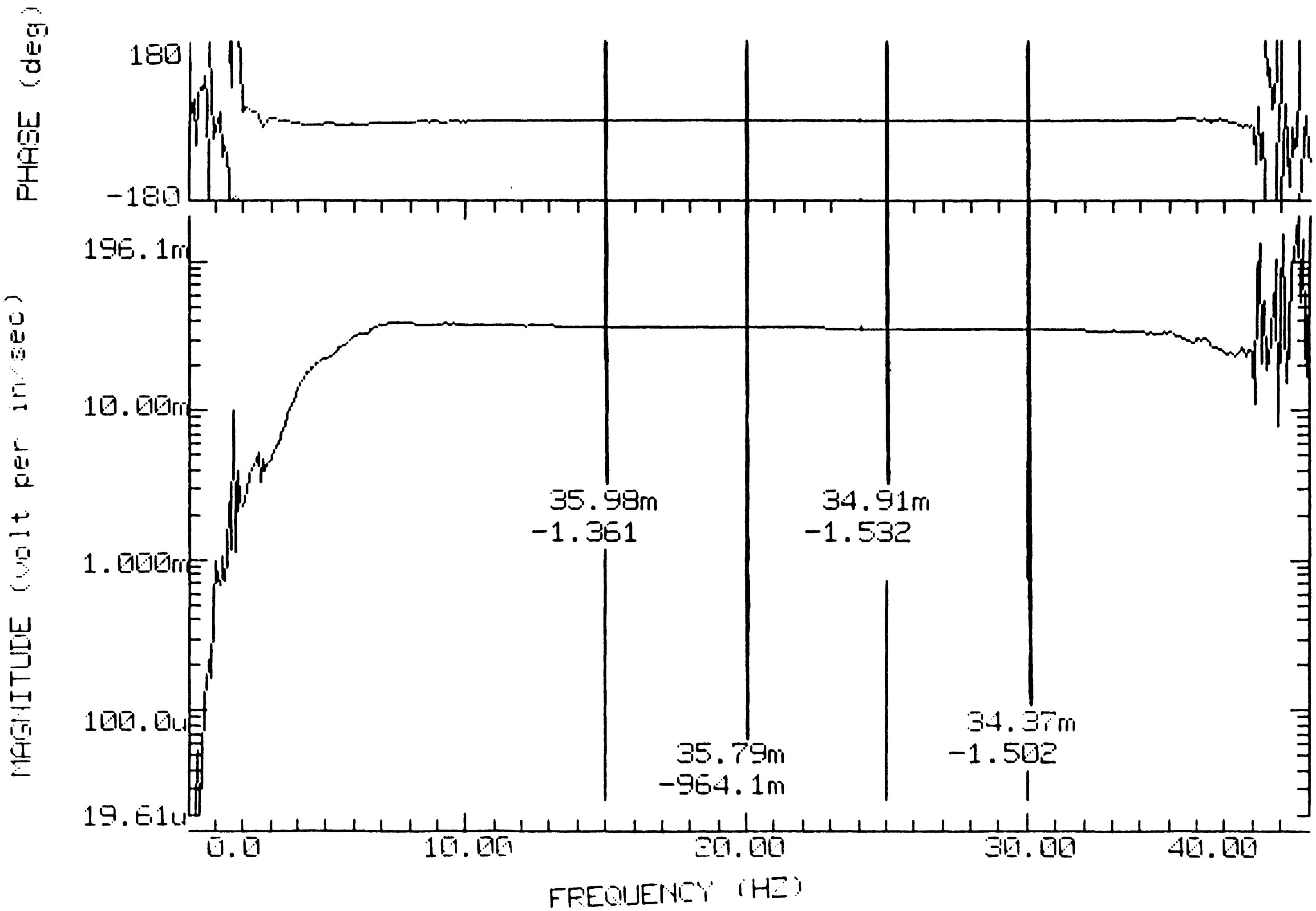

Figure 6: Calibration curve for a velocity sensor. The data was smoothed using SM51. Frequency resolution was 0.0781 Hz. The numbers listed are the magnitudes in volts per in/sec and the phases in degrees.

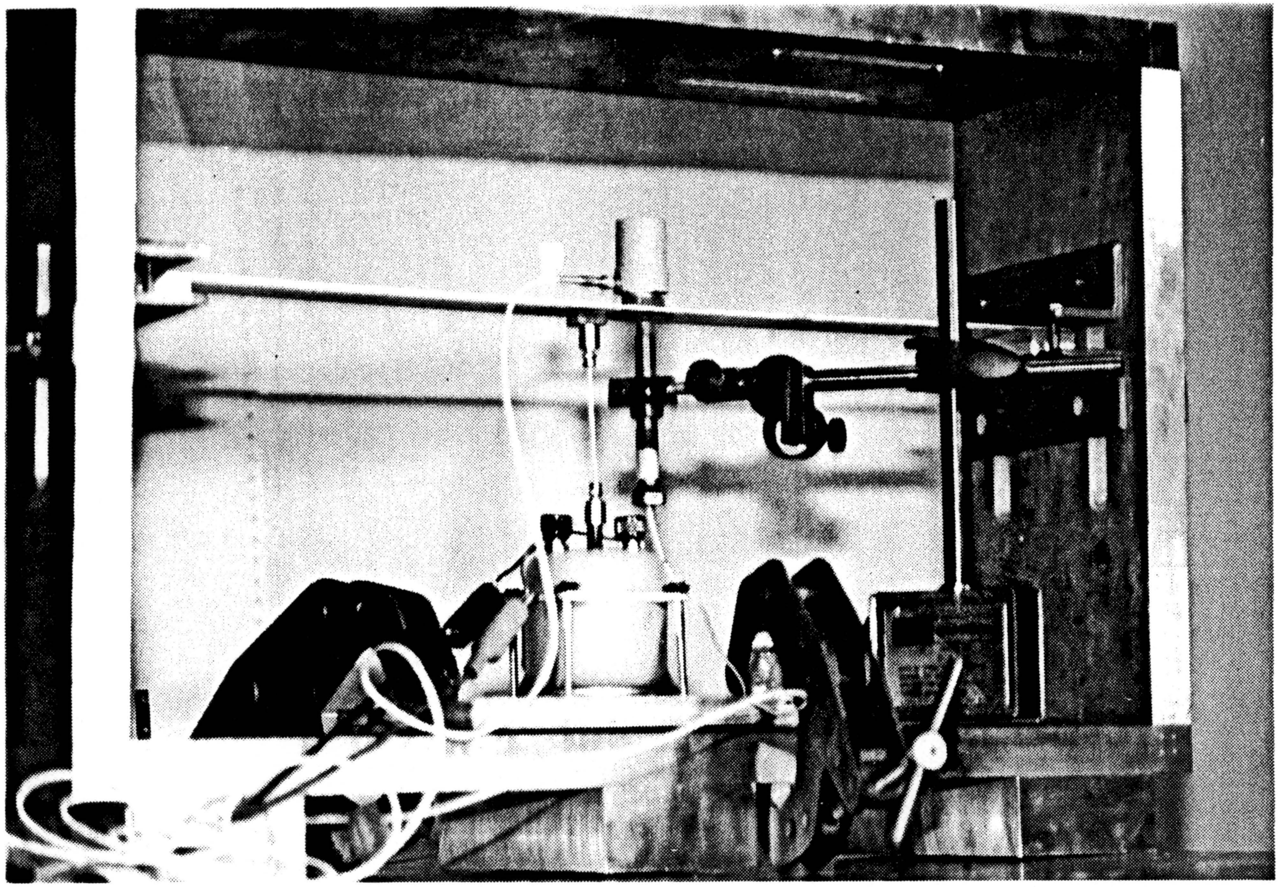

Figure 7: Photograph of the calibration apparatus set up for the calibration of a Bently-Nevada proximity probe.

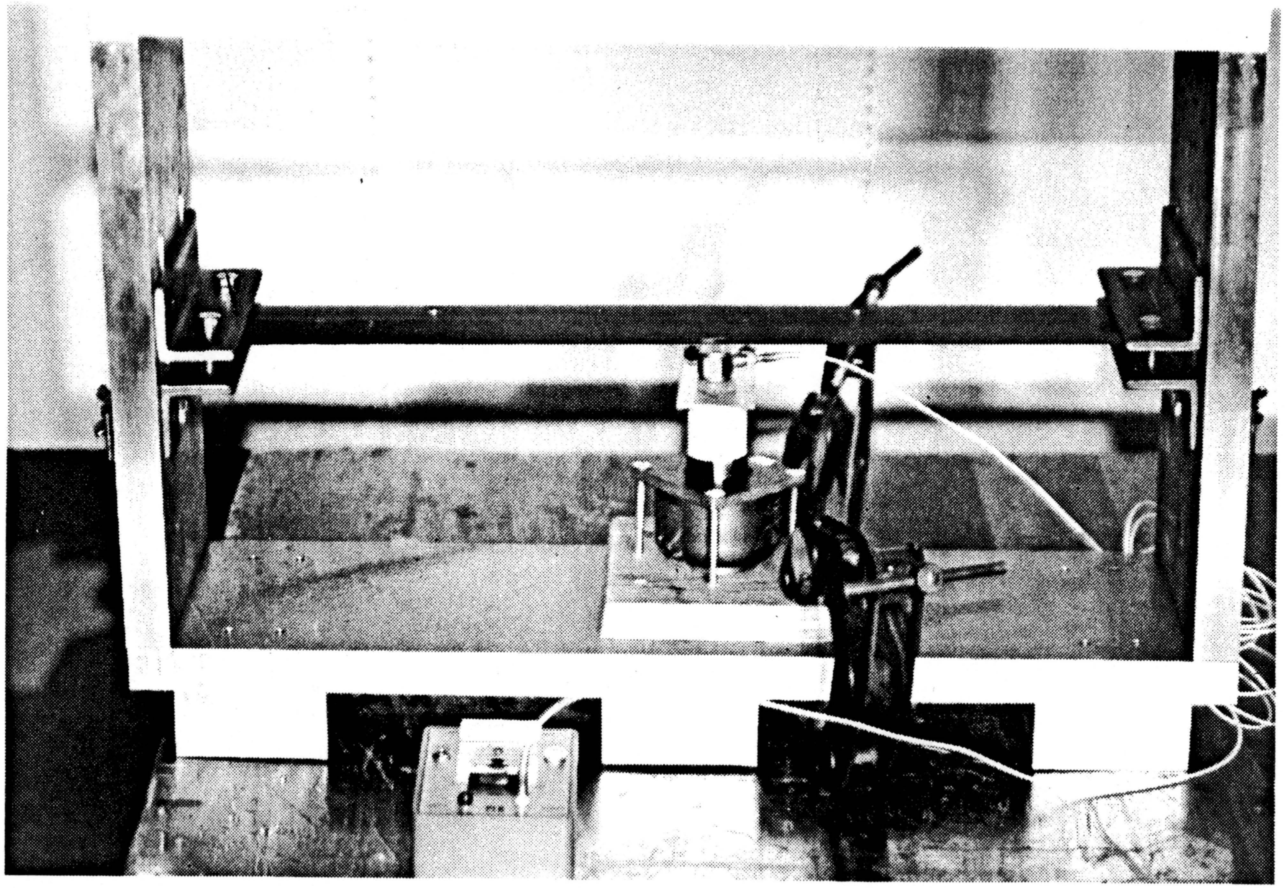

Figure 8: Photograph of the calibration apparatus set for the calibration of a force actuator.

Chapter III

DEVELOPMENT OF EXPERIMENTAL-THEORETICAL MODELS

In order to approximate more of the dynamic characteristics of a LSS, it was necessary to modify an existing beam-cable laboratory structure (Ref. 3) so that along with a number of low-frequency modes, two modes whose frequencies were close would be produced. The beam-cable structure is modeled by eight 10-inch long beam elements representing the vertical beam and string-in-tension elements representing the supporting cables. Figure 9 is a line drawing of the finite element model for the beam-cable structure. The beam-cable model has five natural frequencies under 30 Hz without any closely spaced frequencies. To generate the closely spaced frequencies, a horizontal crosspiece was added to the vertical beam. The crosspiece consisted of a light aluminum beam with lumped masses on both ends.

3.1 DESIGN AND PLACEMENT OF THE CROSSPIECE

A simple finite element model was developed for the symmetric crosspiece. Only the symmetric bending modes of the crosspiece were considered, ignoring the antisymmetric modes which cause torsional motion of the vertical beam.

Antisymmetric motion was not considered because it could not be excited or controlled by the existing control system. The crosspiece was modeled, only for this very preliminary study, as a one-element, two degree-of-freedom (DOF) cantilevered beam with an end mass. The length of the cantilevered beam and the value of the end mass were then varied in order to determine a combination that would produce a fundamental natural frequency around 9 Hz. The crosspiece designed in this manner would be added to the beam-cable structure, which already had a natural frequency around 9 Hz, producing two natural frequencies near 9 Hz.

The implementation of this strategy was first done theoretically. Instead of adding a beam element at right angles to the vertical beam to represent the crosspiece, a two DOF spring-mass element was added. The stiffness of the spring and the mass distribution for the model of the crosspiece were determined from a two-DOF Rayleigh-Ritz analysis of the crosspiece (see Appendix B).

Originally the crosspiece was placed on the vertical beam 20 inches down from the top of the beam at grid point 3 on the vertical beam. The crosspiece could be placed only at a location corresponding to a grid point in the finite element model. This configuration produced closely spaced modes, but it was determined that one of these modes was not well suited for control experiments. This mode was basically uncontrollable because it was a very localized appendage mode of the crosspiece, involving very little motion of the vertical beam in the region where the controllers could be placed. Therefore, a study was conducted to determine the best position for the crosspiece among the nine equally spaced grid points along the vertical beam.

This study revealed that there were only two candidate grid points at which the crosspiece could be attached to produce the closely spaced natural frequencies. These positions were the initial location 20 inches down from the top and the corresponding position 20 inches up from the base of the vertical beam. The second of these locations was more desirable since it produced a more controllable mode. This mode involved more motion of the vertical beam in the region where the sensor-actuator pairs could be located than the corresponding mode with the crosspiece located 20 inches down from the top. Figure 10 is a photograph of the lower portion of the beam-cross-cable structure. In this photograph, the vertical beam, the crosspiece and a tip mass, the lower supporting cables, and the three pairs of colocated velocity sensor-force actuators can be clearly seen.

3.2 FINITE ELEMENT MODEL

A finite element model was developed for the beam-cross-cable system with the MAPMODES computer program. (See Appendix B for an explanation of the MAPMODES program and the input MAPMODES file.) The model had eight 10-inch beam elements for the vertical beam, two string-in-tension elements for the cables, and the linear spring-mass element developed with the Rayleigh-Ritz model to represent the crosspiece. This model also includes two one inch rigid inserts to model the increased stiffness of the vertical beam caused by the clamp holding the crosspiece to the vertical beam. Figure 11 is a close-up photograph of the clamp holding the crosspiece to the vertical beam. Note the Bently-Nevada proximity probe in the lower part of the photograph. The rigid inserts were placed at the bottom of the sixth beam element and at the top of the seventh beam element. Figure 12 is a line drawing of the beam-cross-cable structure modeled by the MAPMODES program. The finite element model is represented by Figure 13; note the spring-mass element representing the crosspiece and the rigid links modeling the clamp. The first six natural frequencies produced by this model are presented in Table 1. Note that all six natural frequencies are under 25 Hz, thus meeting the requirement for low natural frequencies; also note that the fourth natural frequency is only 7.3% above the third natural frequency.

3.3 EXPERIMENTAL NATURAL FREQUENCIES

The STI data acquisition and analysis system with the VAMP software described in Chapter 2 was used to collect and analyze the experimental data. Since the first six natural frequencies were all predicted to be less than 30 Hz, the anti-aliasing filters on the data acquisition unit were set at 30 Hz. Data was collected by the DAAS at 80 samples/sec producing a Nyquist frequency of 40 Hz. The analysis software performs a 1024 point FFT, which gives 512 discrete frequencies in the 0-40 Hz range. The frequency resolution was 0.0781 Hz. Frequency response functions (FRFs) obtained through random excitation revealed that the resonances were extremely sharp with very low inherent passive damping (Figure 14). With these sharp peaks, it was necessary to do a very narrow band study around each of these natural frequencies, in order to accurately determine each resonant frequency. These narrow band studies were done using a VAMP processor command called SWIFT. The SWIFT command causes a narrow band incremental sinusoidal sweep to be generated. The excitation will continue at a discrete frequency for as many cycles as is specified before increasing to the next discrete frequency in the sweep. Frequency resolution can also be controlled using this command. Each of the first six natural frequencies was tested with this narrow band procedure at a frequency resolution of 0.0125 Hz or less. While this testing was proceeding, the force and velocity signals were displayed on an oscilloscope in the X-Y plotting mode. This method of presentation is called a Lissajous Figure (Ref. 5). When the structure is excited at a resonant frequency, the force and velocity are exactly in phase. On a Lissajous figure, this would be indicated by a straight line in the first and third quadrants going through the origin. When the structure is not at resonance the force and velocity signals form a skewed ellipse. If the force is displayed against the displacement, the trace, at resonance, will form an ellipse aligned with the display axes. Off resonance the ellipse will be skewed from the axes.

These results displayed excellent agreement between the theoretical analysis and the dynamics of the real structure. Both the theoretically predicted and the experimentally determined natural frequencies are listed in Table 1. The maximum difference is -2.42% in the first mode. The natural frequencies measured for the structure were very sensitive to the amount of tension in the vertical beam. Normal temperature variation in one day caused the building to expand or contract enough to change the first two natural frequencies as much as 10%. So once good agreement in frequency was obtained between experiment and theory, the tension in the vertical beam and supporting cables was adjusted until the frequencies matched what was previously measured. This adjustment was accomplished by tightening or loosening turnbuckles that attached the bottom cables to the floor.

The primary objectives of this model development were first to create a theoretical model of a structure with a pair of closely spaced modes by a simple modification of an existing model, and second, to modify the existing physical model correspondingly. A theoretical model was developed with close modes at 8.80 and 9.49 Hz. The physical model was modified and the FRFs demonstrate a pair of closely spaced modes was achieved, Figure 14. The theoretical model accurately predicted all of the first six natural frequencies.

TABLE 1

THEORETICAL AND EXPERIMENTAL NATURAL FREQUENCIES

MODE #	FREQUENCIES (Hz)		PERCENT DIFFERENCE
	Theoretical	Experimental	
1	1.853	1.899	-2.42
2	4.803	4.771	0.67
3	8.799	8.719	0.92
4	9.490	9.404	0.91
5	14.44	14.71	-1.85
6	22.73	22.55	0.80

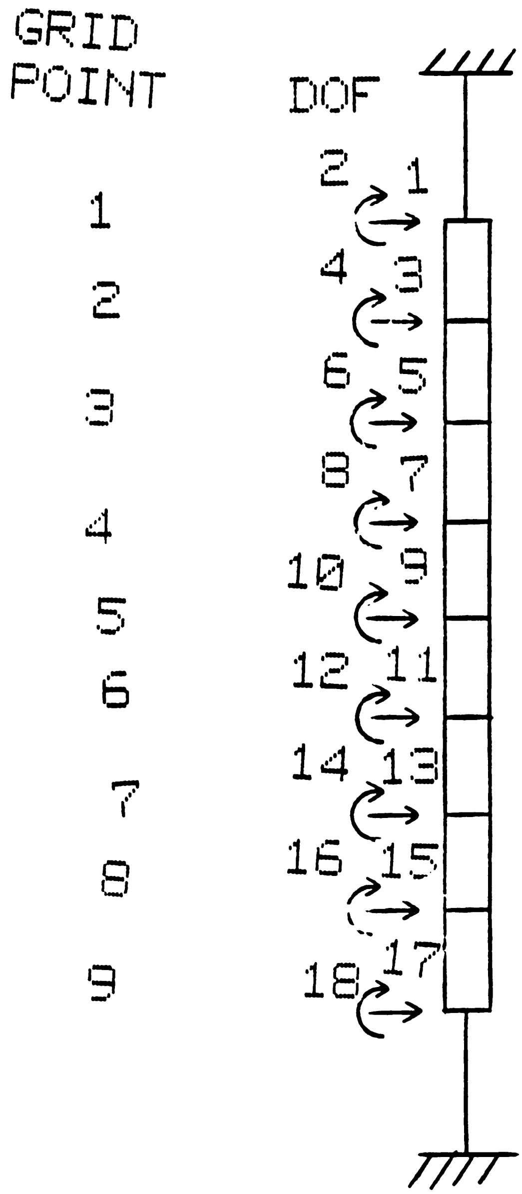

Figure 9: Line drawing of the finite element model for the beam-cable structure. Note the grid point numbering.

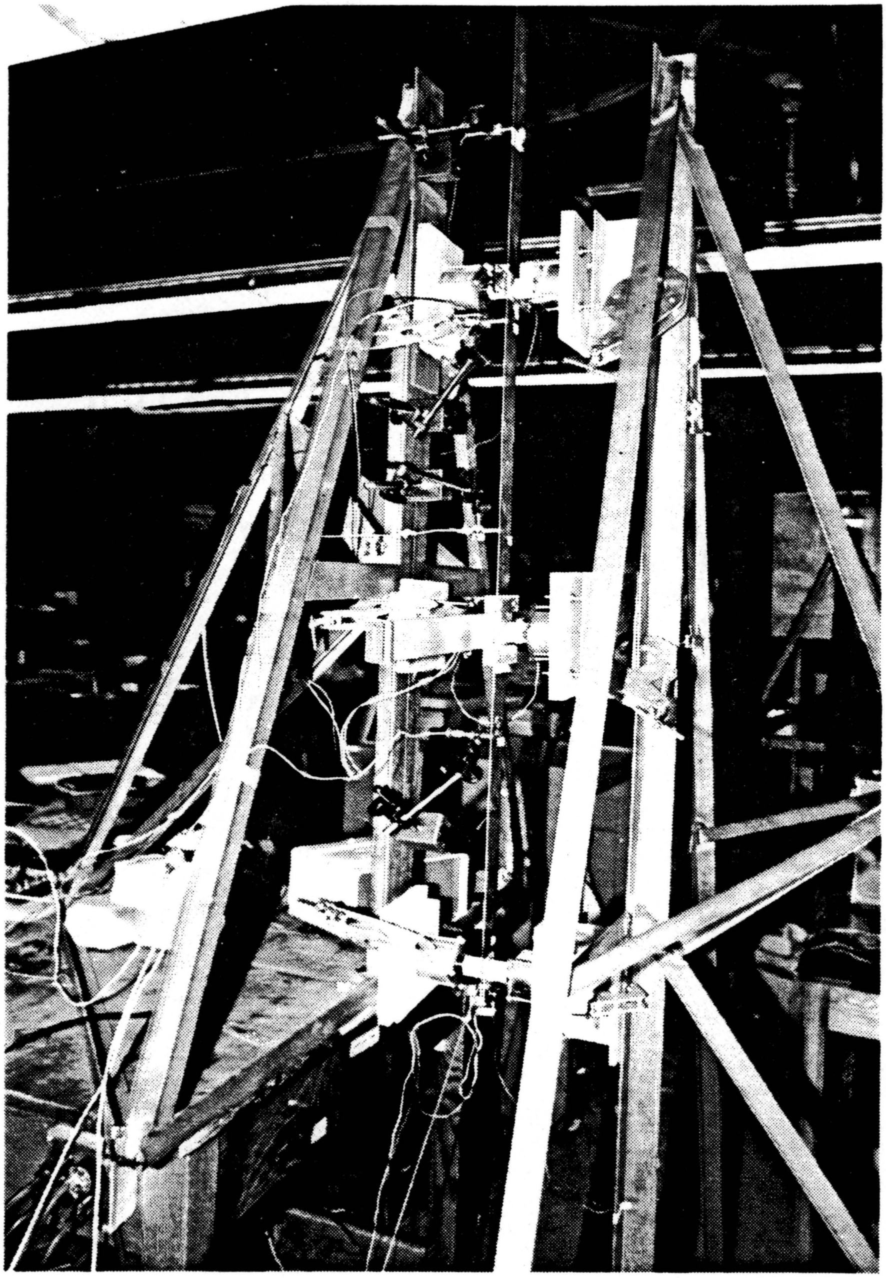

Figure 10: Photograph of lower portion of beam-cross-cable structure showing vertical beam, crosspiece, and lower cables.

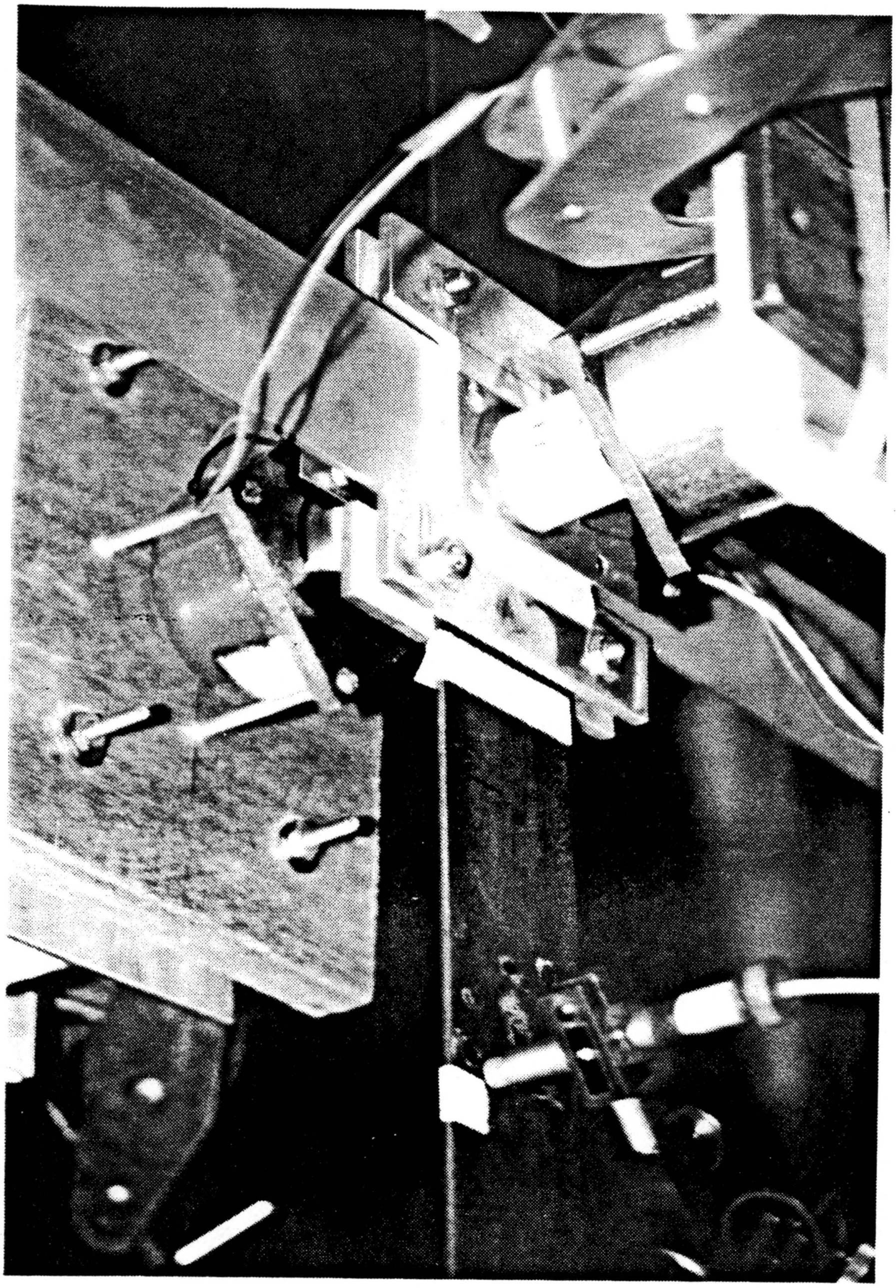

Figure 11: Close-up photograph of clamp holding crosspiece to vertical beam. Note proximity probe in lower part of photo.

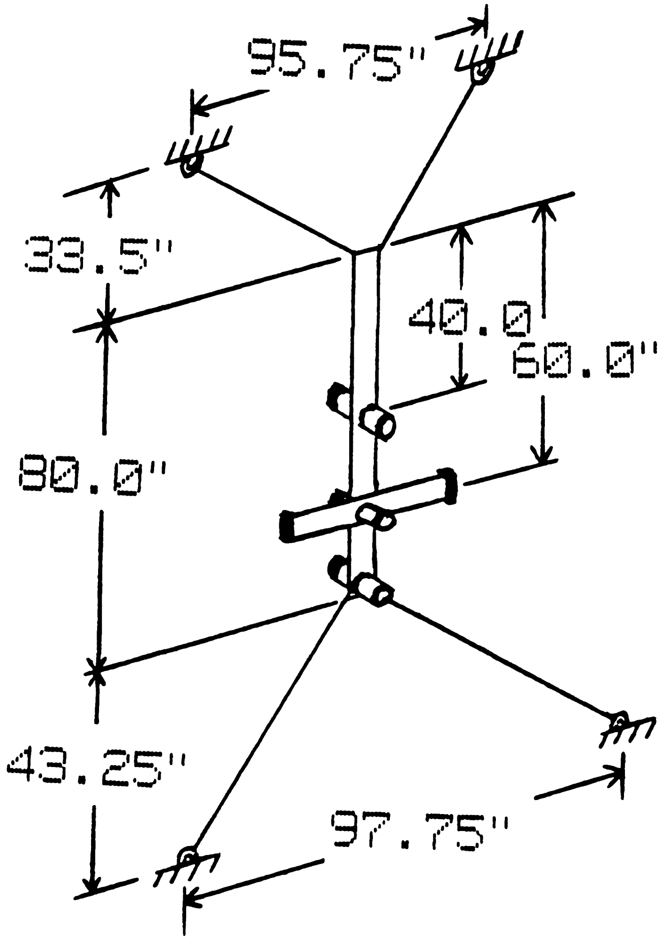

Figure 12: Line drawing of beam-cross-cable structure showing the final location of the crosspiece.

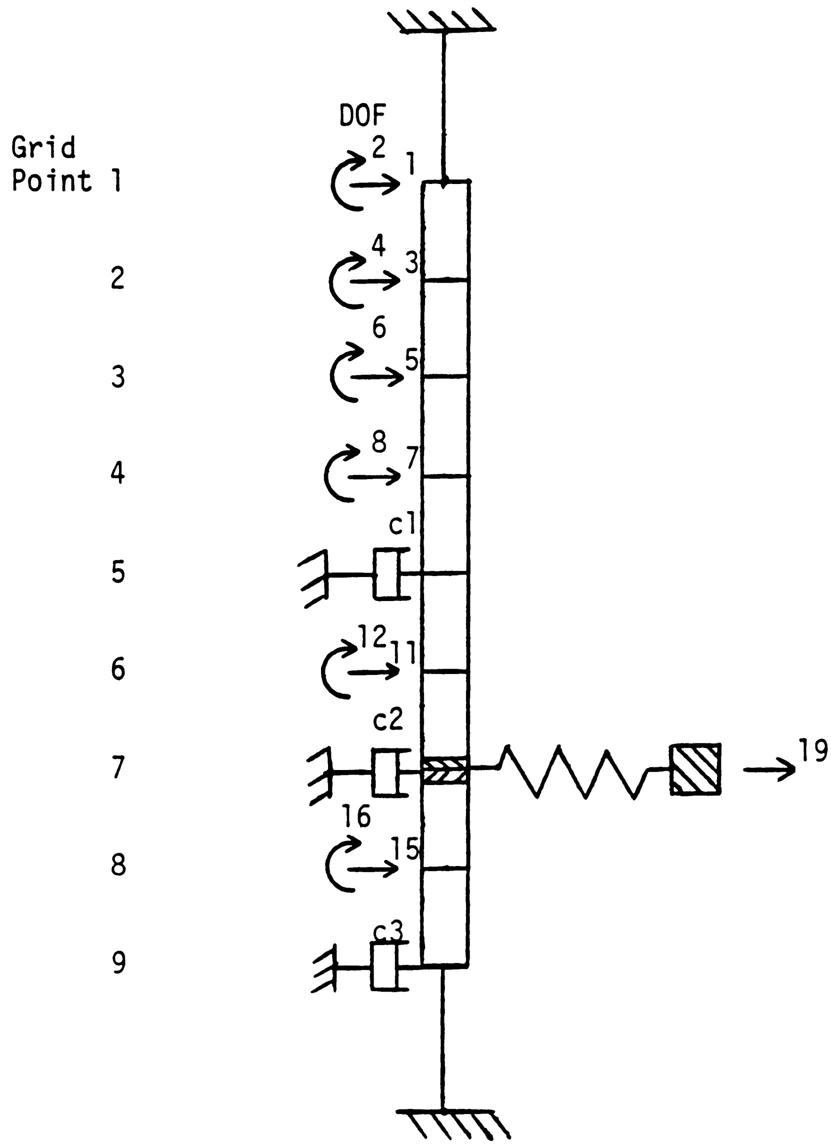

Figure 13: Finite element model of the beam-cross-cable structure. Note spring-mass representation of crosspiece.

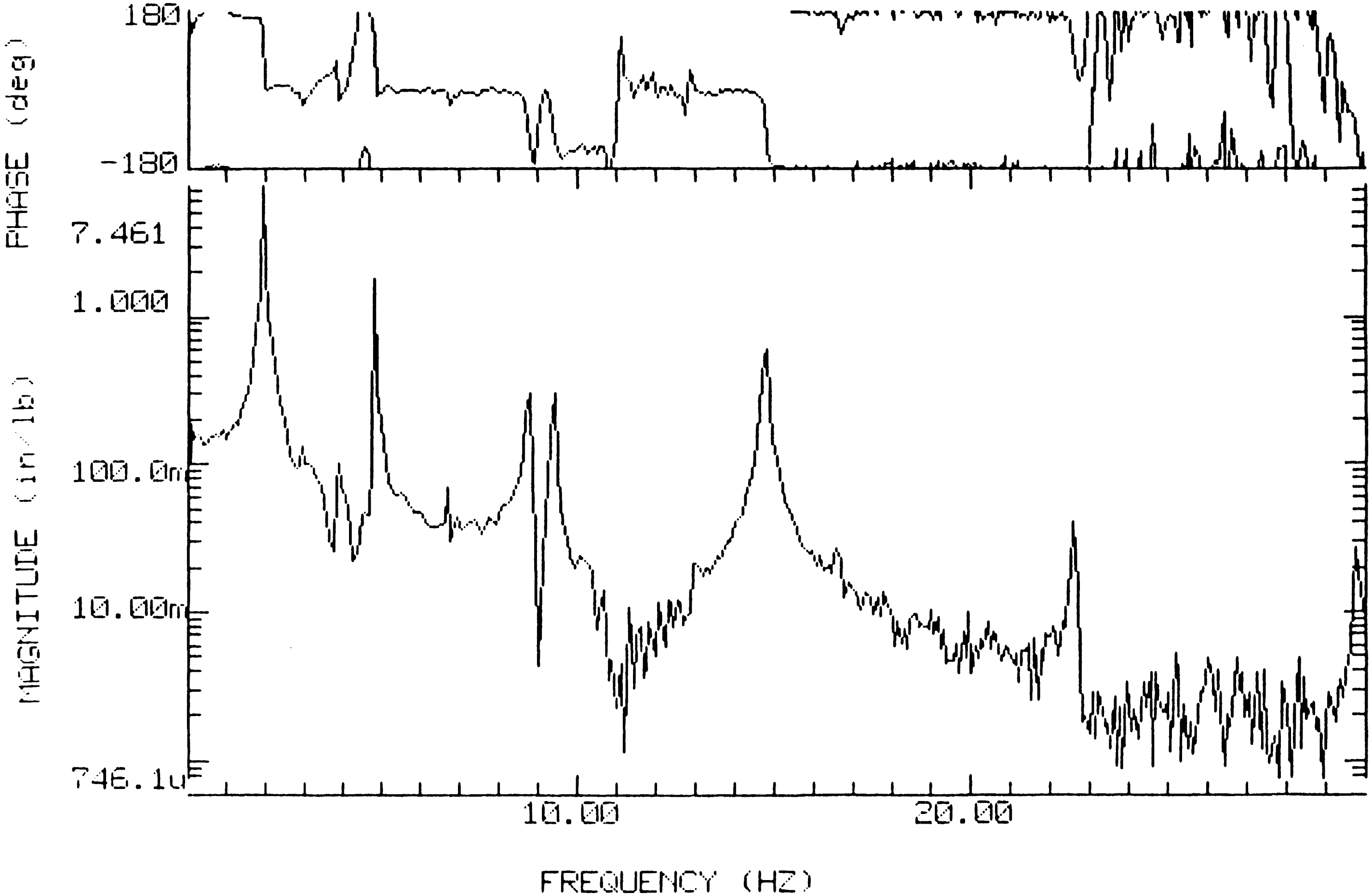

Figure 14: Displacement FRF of beam-cross-cable structure at 54 inches from top, excitation at grid point 9. Note sharp peaks and closely-spaced modes.

Chapter IV

MODE SHAPE TESTING

Chapter III described the development of the beam-cross-cable structure and the verification of the modal frequencies. The next step in the verification of the finite element model is the determination of the accuracy of the structural mode shapes. The predicted mode shapes must be accurate because they can critically affect the design of a control system. If the mode shapes are not accurate the theoretical prediction for the amount of active damping produced by a control design will not match the damping actually produced by that design.

4.1 EXPERIMENTAL APPARATUS AND PROCEDURES

The motion of the vertical beam was sensed at four locations. These four locations were uniformly spaced 12 inches apart starting at 42 inches from the top of the beam. Thus, the second sensor was located at 54 inches, the third at 66 inches, and the lowermost at 78 inches from the top of the vertical beam. The Bently-Nevada proximity probes mentioned earlier were used to sense the deflection of the vertical beam.

To get an accurate measurement of the mode shape, the SWIFT function in the VAMP software was used to excite the structure at discrete frequency intervals around each modal frequency. Modes 1,3, and 4 were excited at grid point 5, the center of the beam, since these modes had their maximum response on the vertical beam near that point. Mode 2 was excited at grid point 9, the base of the beam, for the same reason. The forcing signal was also acquired by the data acquisition system.

FFTs of both the response data and the forcing function were calculated and then the FFT of the displacement response was divided by the FFT of the forcing function to produce the displacement FRF.

The curve fit routine available in the standard VAMP software has the ability to fit a number of FRFs at the same time and then calculate a global average for all the FRFs. The curve fit routine calculates the frequencies and damping ratios for each mode in each FRF and then calculates a global average. This routine also calculates the relative amplitudes and phases at resonance for each mode in each FRF giving the values as the mode shape for the FRF. A cubic polynomial was then fit to the four points at which the motion was measured so that the mode shapes for the lower half of the vertical beam could be interpolated. Only the first four modes were tested because the more complex higher modes could not be adequately defined by only four data points.

4.2 RESULTS AND COMPARISON WITH THEORY

The first time this modal testing was done on the beam-cross-cable structure, a discrepancy was found between the theoretical shape of the first mode and the experimental shape. Much more bending was present in the vertical beam than was predicted by the finite element model. The bending stiffness of the vertical beam was the first property suspected of causing this inaccuracy. Therefore, the bending stiffness was checked experimentally, as described in Appendix C. The actual EI value was determined to be 9060 lbs-in^2 as compared with the original value of 9829 lbs-in^2. This value was changed in the finite element program and the beam tension in the program adjusted until the natural frequencies again matched the experimental values. Also, the bending stiffness of the crosspiece beam was tested and corrected in the program.

The modal tests were then performed again and compared with the theoretical predictions with much better agreement. Figure 15 contains plots of modes 1 and 2 with both the theoretical and experimental mode shapes presented. Figure

16 displays both experimental and theoretical modes 3 and 4. Figure 17 has only the theoretical mode shapes for modes 5 and 6 since these modes were not measured experimentally. The experimental mode shapes were scaled to match the theoretical mode shapes at the center of the vertical beam for ease in comparison. Notice that on the plots the entire theoretical mode shape is plotted including the position of the end of the crosspiece, but only the lower half of the beam is represented by the curvefit to the experimental data. The cables-in-tension are not represented in any of the mode shape plots. Good agreement between the experimental and theoretical mode shapes has been obtained for all four of the modes tested.

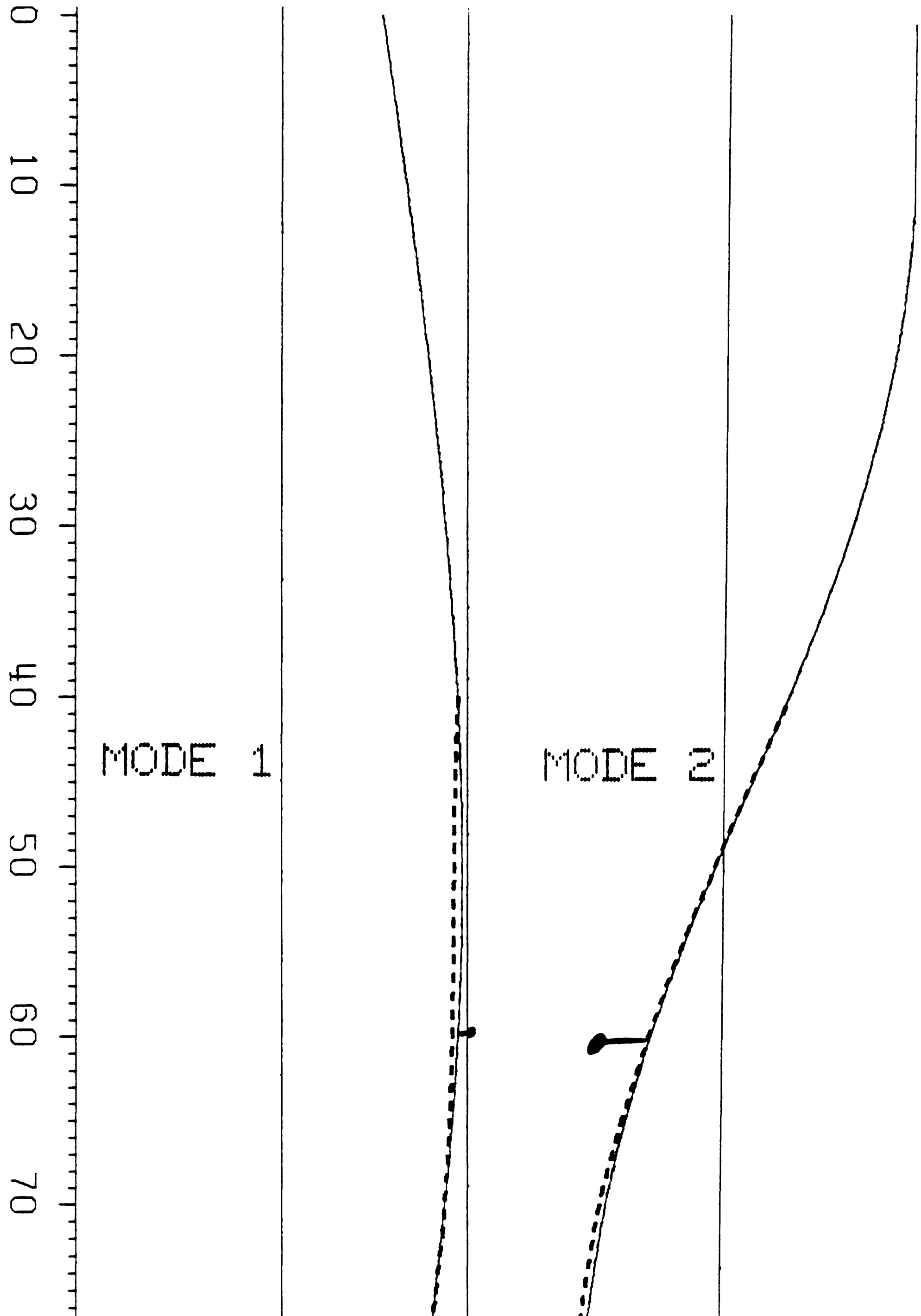

Figure 15: Beam-cross-cable modes 1 and 2. Theoretical mode shape: solid line. Experimental mode shape: dashed line.

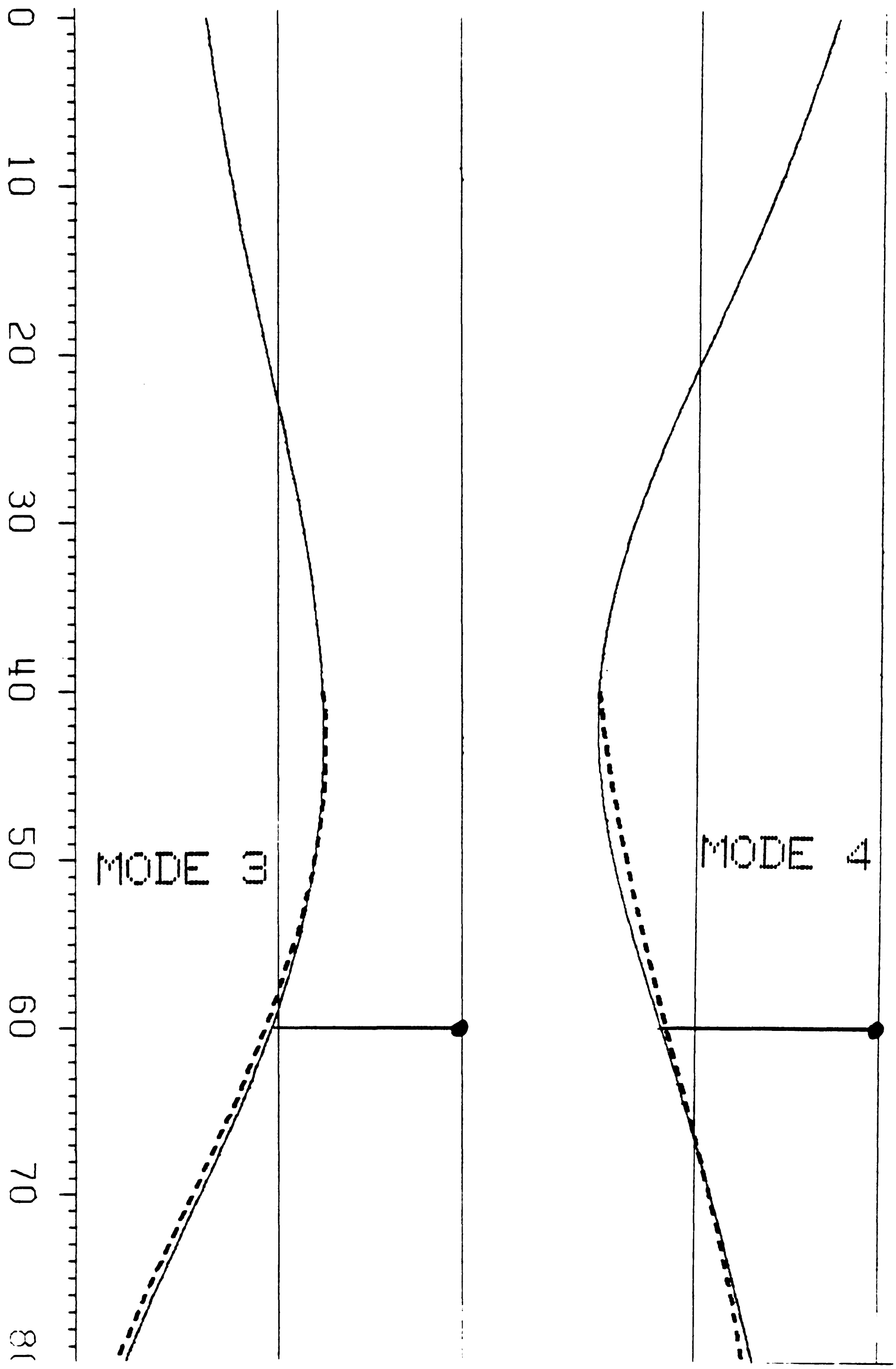

Figure 16: Beam-cross-cable modes 3 and 4. Note low level of response on vertical beam compared to crosspiece response.

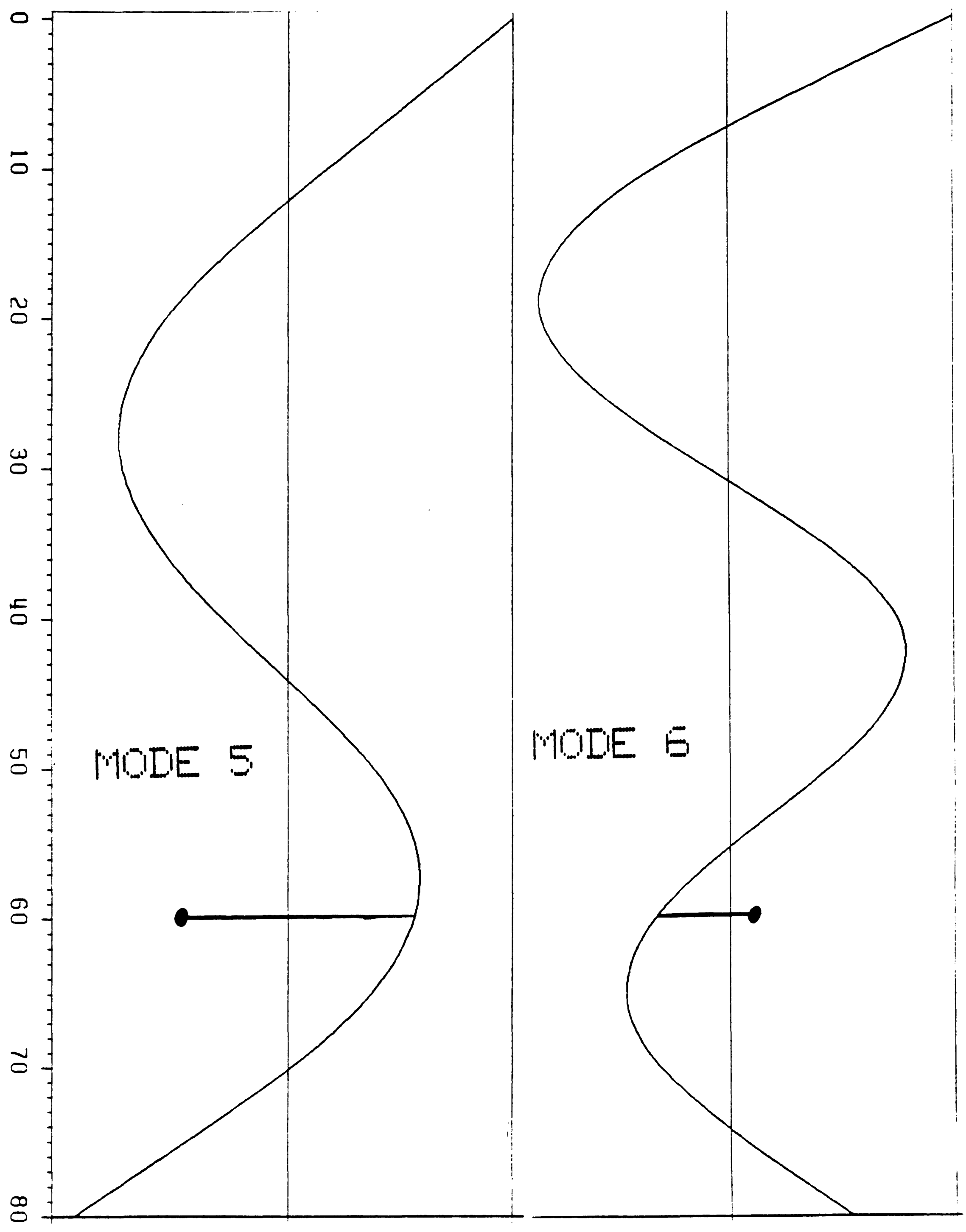

Figure 17: Beam-cross-cable modes 5 and 6. Theoretical mode shape only.

Chapter V

EXPERIMENTAL VALIDATION OF CONTROLLED SYSTEM BEHAVIOR

5.1 BEAM-CABLE STRUCTURE

The first work done on the experimental validation of the results of optimization of a control system-structure combination was done using the original beam-cable structure described in Reference 3. The results of the optimization and the experimental validation have been published in Reference 6.

The control system for this beam-cable structure consisted of one colocated velocity sensor-force actuator pair located at the lowermost end of the beam. In this case, the optimization of the control system was just the determination of the feedback gain strength (directly comparable to a viscous dashpot constant c) needed to produce a minimum damping ratio of 0.03 in the first five structural modes. The optimization of the structure was intended to reduce the control strength needed to maintain that minimum damping ratio. The structure was modified by allowing lumped masses to be placed at any of the nine grid points on the beam (Figure 9). The total added mass was constrained to 10% of the beam mass or less. The greatest reduction in control strength needed to maintain the minimum damping ratio occurred when all 10% of the added mass was placed at grid point 8 of the finite element model.

Two cases, the baseline design and the added mass design, were verified experimentally. Velocity-to-force FRFs were measured on the beam-cable structure. Values for the modal damping ratios and modal frequencies were then inferred from the data. These experimentally determined values were then compared with the theoretical predictions.

Figure 18 is a schematic diagram of the experimental apparatus. Random force excitation was used to drive the structure at one of two points on the structure. The structure either was forced at grid point 9 through the same coil acting as the control actuator or it was forced at grid point 8 using a shaker (Figure 19). For forcing at grid point 8, the excitation signal e(t) from the DAAS was directed into a power amplifier, which drove the shaker. Using the control actuator coil also as the driver was slightly more complex. A simple summing circuit was required to add the excitation signal to the control feedback signal. Figure 20 is a diagram of the circuits used to apply the gain G and sum the control feedback signal with the excitation signal. The voltage output of the summing circuit went to a controlled current power amplifier with a transduction constant of K = 0.25 Ampere/Volt (Ref. 3). The controlled current power amplifier was desired rather than the more customary controlled voltage power amplifier so that the effect of the motion induced voltage in the actuator coil would be nullified.

The control feedback signal was produced by taking the voltage produced by the motion of the sensing coil, putting it through a high impedance buffer and then through an analog gain circuit (Figure 20). An integrated circuit operational amplifier with an extremely high input impedance was used as the buffer. The buffer was needed to minimize the current flow through the velocity sensing coil.

A coil moving with velocity $\dot{u}$ in a magnetic field generates a voltage $C_v \dot{u}$ and a coil carrying a current i in a magnetic field produces a force C_f i, with C_v and C_f being the calibration constants for the velocity sensor and force actuator respectively. Therefore, the force generated by the current output from the controlled current power amplifier is $F = C_f K (-G C_v \dot{u} + e(t))$ The calibration constants are accurate for displacements less than approximately 0.1 inch from equilibrium. The relationship between the viscous damping constant c and the control gain G is $c = G K C_v C_f$. Control gains are calculated using this equation when the damping constant c is specified.

For generating data, a random excitation signal e(t) was used with the general level set as high as possible consistent with keeping the maximum displacement within the linear range of the sensor-actuator pair. A good signal-to-noise ratio was achieved with this strategy. FFTs of both the velocity response and the force excitation were calculated. The velocity-to-force FRF was produced by dividing the FFT of the velocity response by the FFT of the force excitation. The frequency resolution of the FRF was 0.0781 Hz. Data obtained from a single excitation period, without windowing, produced FRFs that were reasonably smooth and reproducible. Therefore neither averaging nor windowing were used.

The experimental FRFs were analyzed with a curve fitting routine in the standard VAMP software. This curve fitting routine was based on a five mode theoretical model, and it fit frequency, amplitude, and damping ratios simultaneously. The experimental and theoretical FRFs for both the baseline and the added mass cases are presented in Figure 21. Experimental FRFs are the solid curves and theoretical curve fits are the dashed curves. The curve fits are clearly very accurate, deviating significantly from the experimental results only above the fifth natural frequency. The deviation of the theoretical curve fit from the experimental data at frequencies above the fifth mode is due to the absence of a sixth mode in the theoretical model for the curve fit. This had only a negligible effect on the modal frequencies and damping ratios.

The modal damping ratios and the modal frequencies calculated by the curve fit routine are listed with the theoretically predicted values (Ref. 6) for both the baseline and added mass designs in Table 2. Experimental and theoretical frequencies agree quite well for both designs.

Agreement between the theoretically predicted and experimentally determined damping ratios is good, with the differences being explained in part by the absence of inherent damping from the structural finite element model. Accurate inherent damping values proved very difficult to measure because the beam-cable structure is so lightly damped. Despite the difficulties, approximate ranges for the damping values were determined. The inherent damping for the first two modes lay between 0.001 (Ref. 6) and 0.0035 (Ref. 3), for the third mode the range was 0.003 to 0.005, and for the fourth and fifth modes the damping ratios were approximately 0.005. The higher range for the inherent damping in mode 3 may account for the fact that mode 3 has the only experimental damping ratio which is higher than the theoretically predicted damping ratio.

Since the experimental damping ratios are, in general, lower than the theoretical damping ratios, one should immediately suspect that the control system was producing a lower damping constant c than was expected or perhaps the calibration factors on either the velocity sensor or the force actuator were incorrect. Therefore, each of the suspected problem areas were subjected to independent checks. The velocity sensor and the force actuator were recalibrated and the calibration factors obtained matched the ones originally used. The control circuit feedback gain was checked, reset, and checked again. Also, the gains and calibration constants in the DAAS were checked and found to be correct. Finally the experimental data was retaken and new damping ratios calculated, but no significant difference was found.

During the checking procedure, it was discovered that the centerline of the sensor/actuator pair of coils was actually located about 1/4 inch above the lower end of the beam. The coils were relocated so that their centerlines were directly in line with the bottom edge of the beam. The value measured for the fifth damping ratio before moving the coils was 0.020 and after repositioning it was 0.025, the value given in Table 3. This increase was caused by the steep gradient in the mode shape of mode 5 at grid point 9.

Therefore, the small change in position produced a significant change in the active damping applied to that mode.

5.2 BEAM-CROSS-CABLE

The next stage of the work was to advance to a more complex model and control system. Chapter III describes in detail the development of the beam-cross-cable finite element model and the subsequent verification of the first six natural frequencies. The first four open-loop mode shapes were also verified experimentally, as was discussed in Chapter III. For a more advanced control system, three pairs of colocated sensor-actuator direct velocity feedback controllers were made available on the structure (Figure 22).

Three different theoretical control system-structure designs were tested experimentally on the beam-cross-cable structure. The baseline design was a simple, uniform gain for each of the controllers. No specific damping ratios were designed for this case. In the second case the sum of the feedback gains was minimized with the constraint that each of the first six damping ratios must be 0.03 or greater. The last design tested was the optimization of the control system and the structure simultaneously (Ref. 7).

As with the beam-cable design, the optimization routine was allowed to put added mass at any of the nine grid points on the vertical beam. The optimization again was to reduce the sum of the feedback constants. All of the added mass was placed at grid point eight, but only 2.0% of the total structural mass was added. This let the control strength of the second controller go to zero while the other two control strengths remained approximately the same. Table 3 is a listing of the control strengths for the three designs.

Instead of using velocity FRFs for the response data, four proximity probes were set up to measure the translations at four points on the lower portion of the beam (Figure 22). In this manner, four different FRFs were measured to provide a larger data base from which to obtain the modal damping ratios. The curve fit routine was given all four FRFs and all six modes to fit at the same time. It fit the first six modes on each FRF and then averaged the four modal damping values for each mode to obtain a global value.

Each of the designs was tested three different times and modal damping values were obtained from each test to check the repeatability of the experiment. Each test consisted of exciting the structure through the lowermost control actuator with a random excitation signal in the same manner as the previous tests. The displacement levels of the vertical beam had to be kept within 0.1 inch from equilibrium so that the sensor-actuator pairs and the proximity probes remained within their linear ranges.

The results obtained from the three test runs made on each design displayed good repeatability and good agreement with the theoretically predicted values for the modal damping ratios. Table 4 is a listing, for example, of the modal damping ratios for each of the three test runs made on the optimized gain design. Table 5 lists the mean damping ratios along with the theoretically predicted values (Ref. 7) for each design. In the parenthesis is the standard deviation as a percentage of the mean. This number is a measure of the repeatability of the experiments. In general, the experimentally determined damping ratios are lower than the theoretically predicted values except for the fourth mode. Some of these differences may be explained in part by the absence of open loop inherent damping in the theoretical model. At this time no other explanation for these discrepancies has been found.

The open loop damping values were measured on the beam-cross-cable structure from open loop displacement FRFs. FRFs were measured at the same places as in the closed loop testing and the curve fit routine performed a six mode global fit on the data to find the open loop modal dampings. Open loop decay tests were also used to verify the damping values for the first two structural modes. These values are 0.0045 for mode 1, 0.0020 for mode 2, 0.0040 for mode 3, 0.0019 for mode 4, 0.0029 for mode 5, and 0.0015 for mode 6. It was discovered that there is some current leakage through the sensor and actuator coils not in use in the open loop testing that was causing some additional modal damping. This additional damping could be eliminated by shorting the coil ends, but this could not be done for the closed loop tests so the additional damping must be considered part of the inherent damping of the structure.

Figures 23 to 26 are the closed loop experimental and theoretical curvefit FRFs for one test of the uniform gain design. The dashed lines are the experimental data and the solid lines are the theoretical curve fits. In each diagram, agreement between the two curves is so close that near the peaks of the resonances only one curve can be seen. The characteristics of the damped mode shapes can be inferred from these plots, especially for the third and fourth modes. The absence of a peak for the fourth mode in the FRF from 66 inches from the top of the vertical beam merely indicates that the location is a nodal point of the fourth mode (see Figure 16). Figures 27 to 30 are the four

FRFs from one test of the optimized gain design. These FRFs exhibit the same general shape as the FRFs for the baseline design but at a generally lower magnitude level. This was to be expected as the optimized gain case was designed to have a higher level of active damping. Again the solid curves are the experimental data and the dashed curves are the theoretical curve fits. The characteristics of the FRFs for the added mass design are much the same as the FRFs from the optimized gain design, as should be expected since both configurations were designed to have the same minimum damping levels.

TABLE 2

MODAL FREQUENCIES AND DAMPING RATIOS FOR BEAM-CABLE

MODE #	BASELINE DESIGN				10% ADDED MASS DESIGN			
	Damping Ratio		Frequency(Hz)		Damping Ratio		Frequency(Hz)	
	Exp.	Theory	Exp.	Theory	Exp.	Theory	Exp.	Theory
1	0.177	0.200	2.5	2.5	0.166	0.125	2.2	2.2
2	0.270	0.314	5.6	5.5	0.166	0.121	5.1	5.0
3	0.169	0.156	8.9	8.8	0.080	0.071	9.2	9.3
4	0.061	0.064	15.2	15.3	0.046	0.049	15.5	15.6
5	0.025	0.030	23.9	24.9	0.025	0.030	23.4	24.2

TABLE 3

CONTROLLER GAIN STRENGTHS (lb-sec/in)

Gain	Uniform Gain Design	Optimized Gain Design	Added Mass Design
C1	0.01188	0.06289	0.06248
C2	0.01188	0.01165	0.00000
C3	0.01188	0.02870	0.09520

TABLE 4

REPEATABILITY OF MEASURED MODAL DAMPING RATIOS FOR THE OPTIMIZED GAIN DESIGN

Mode	Damping Ratios		
	Test Number		
	1	2	3
1	0.214	0.194	0.192
2	0.043	0.039	0.039
3	0.051	0.050	0.050
4	0.032	0.034	0.041
5	0.024	0.024	0.023
6	0.033	0.025	0.028

TABLE 5

EXPERIMENTAL AND THEORETICAL MODAL DAMPING RATIOS

Mode	Uniform Gain Design		Optimized Gain Design		Added Mass Design	
	Experiment	Theory	Experiment	Theory	Experiment	Theory
1	0.068 (1.3)	0.074	0.200 (6.1)	0.219	0.170 (0.7)	0.194
2	0.017 (6.2)	0.018	0.040 (5.7)	0.046	0.041 (1.4)	0.047
3	0.024 (9.7)	0.022	0.050 (1.1)	0.071	0.062 (7.6)	0.074
4	0.010 (4.6)	0.010	0.036 (13.3)	0.030	0.034 (10.5)	0.030
5	0.013 (6.6)	0.013	0.024 (1.9)	0.030	0.022 (0.7)	0.030
6	0.007 (3.5)	0.008	0.029 (14.0)	0.030	0.028 (5.5)	0.030

The experimental modal damping ratio presented is the average of three separate measurements. The value given in parentheses is the percent of the standard deviation of those three measurements relative to the average.

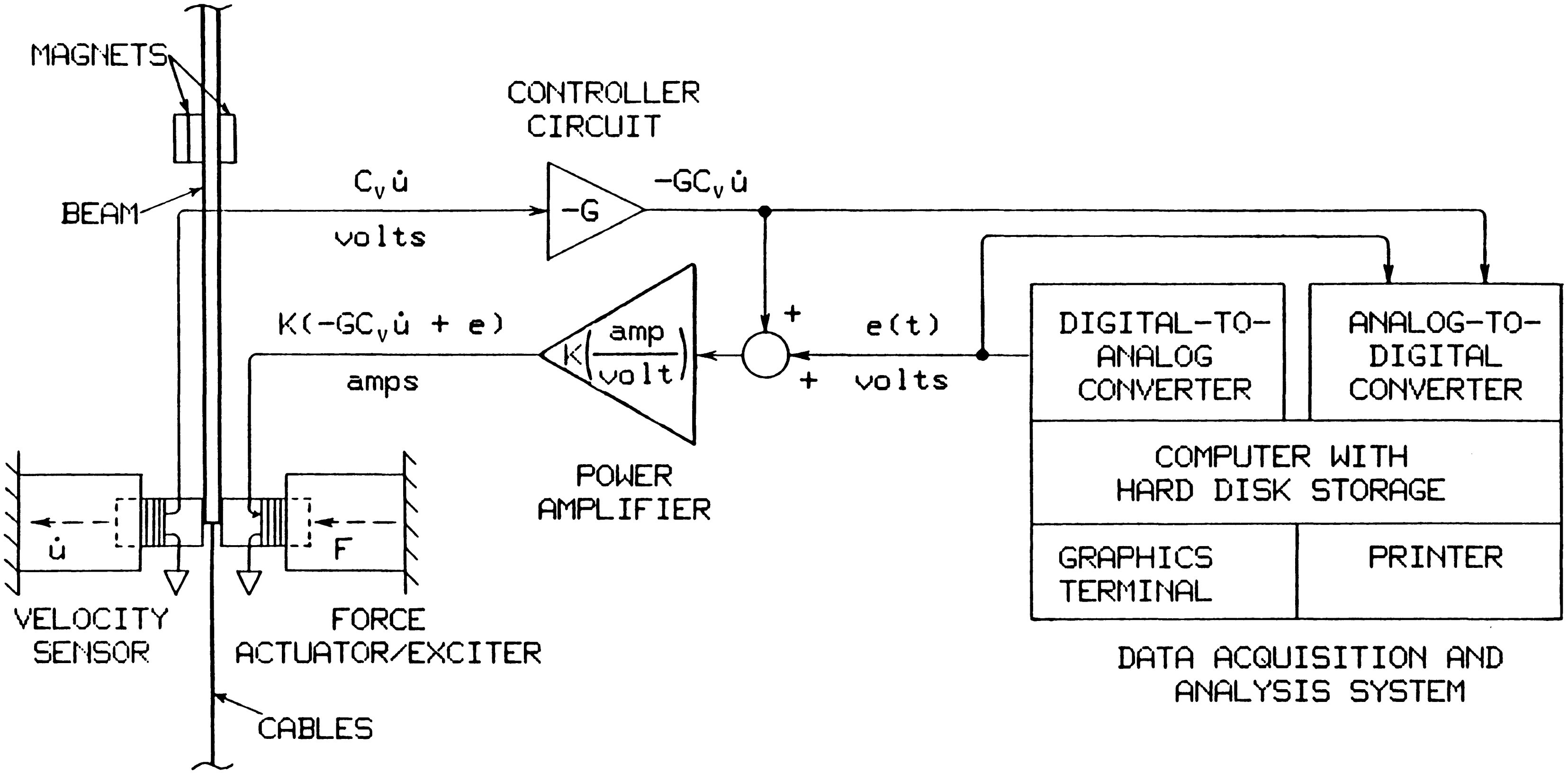

Figure 18: Schematic diagram of experimental apparatus.

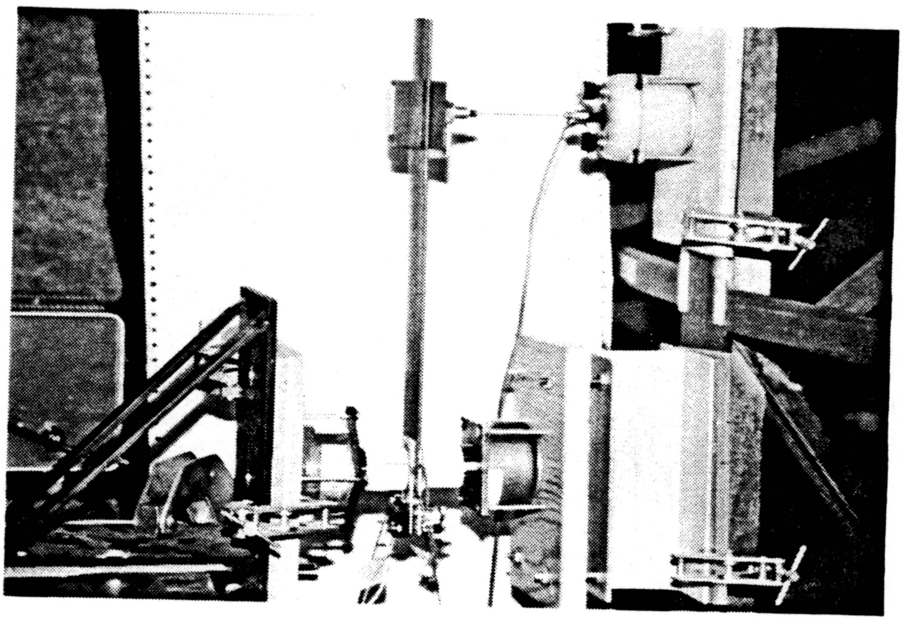

Figure 19: **Photograph of beam-cable structure with shaker and added mass in place.**

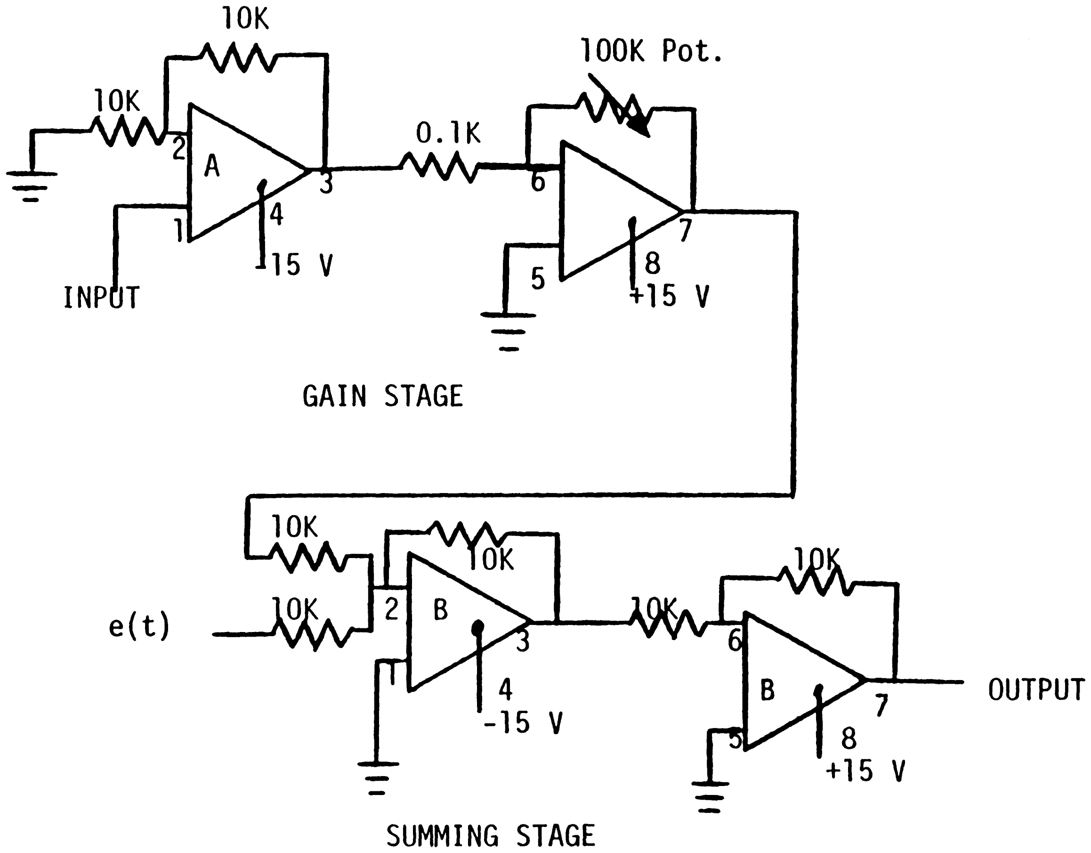

A = 1/2 353 Op. Amp.

B = 1/2 1458 Op. Amp.

Figure 20: Circuit diagram for summing circuit and feedback gain circuit.

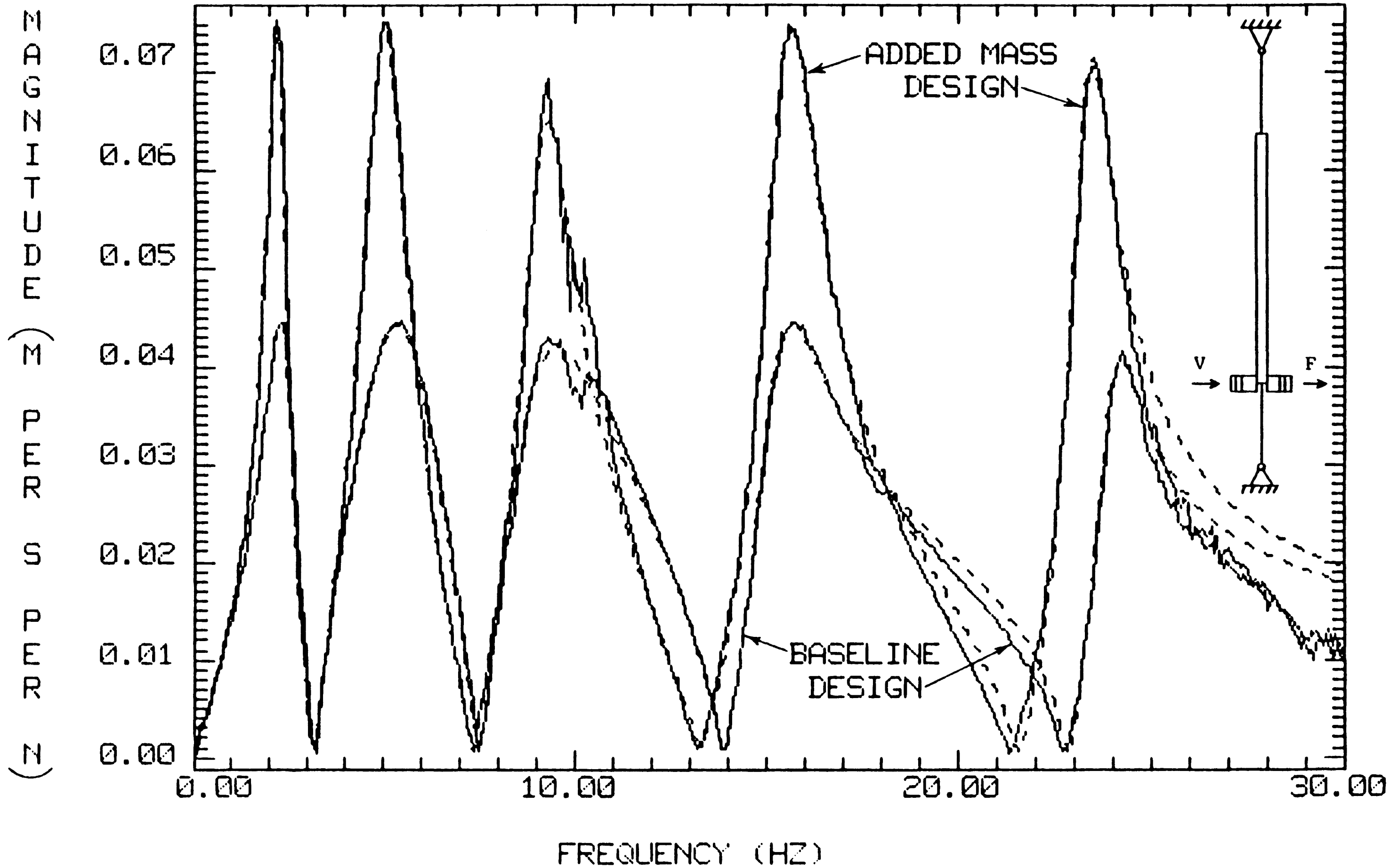

Figure 21: Experimental driving-point frequency response magnitudes for beam's bottom edge.

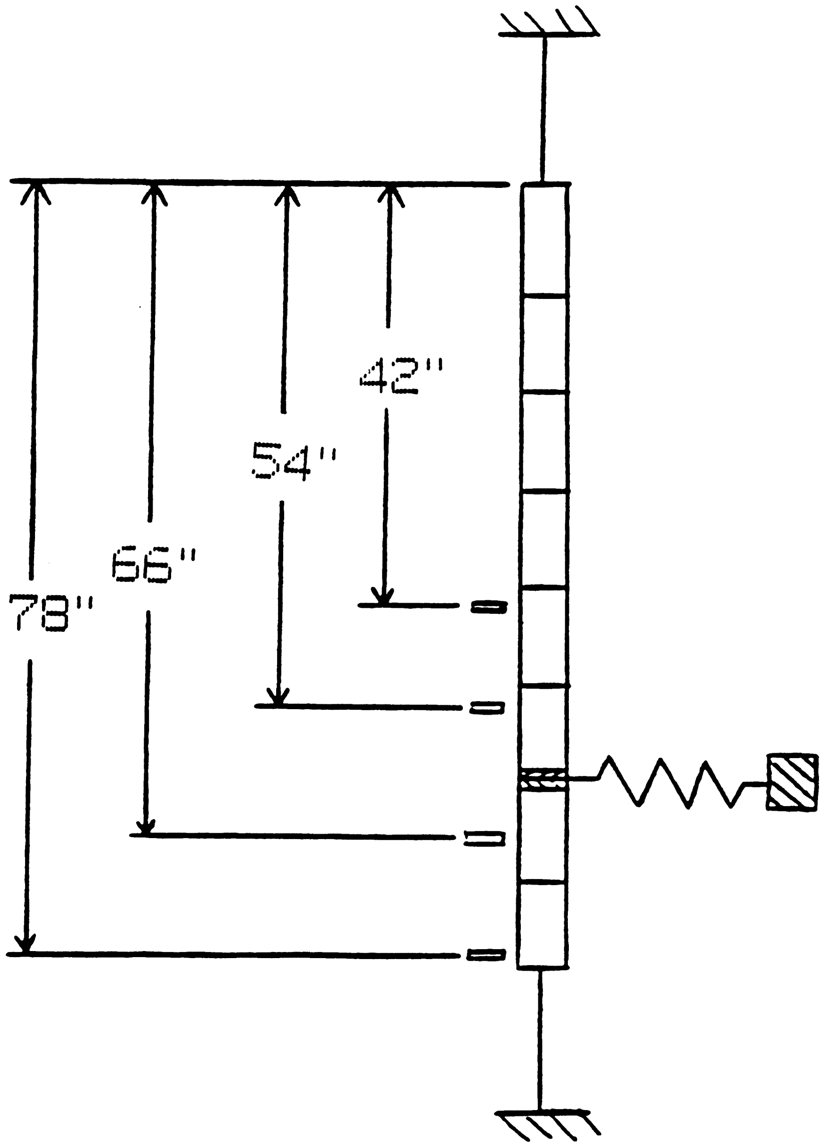

Figure 22: Line drawing of finite element showing locations of displacement sensors on beam-cross-cable structure

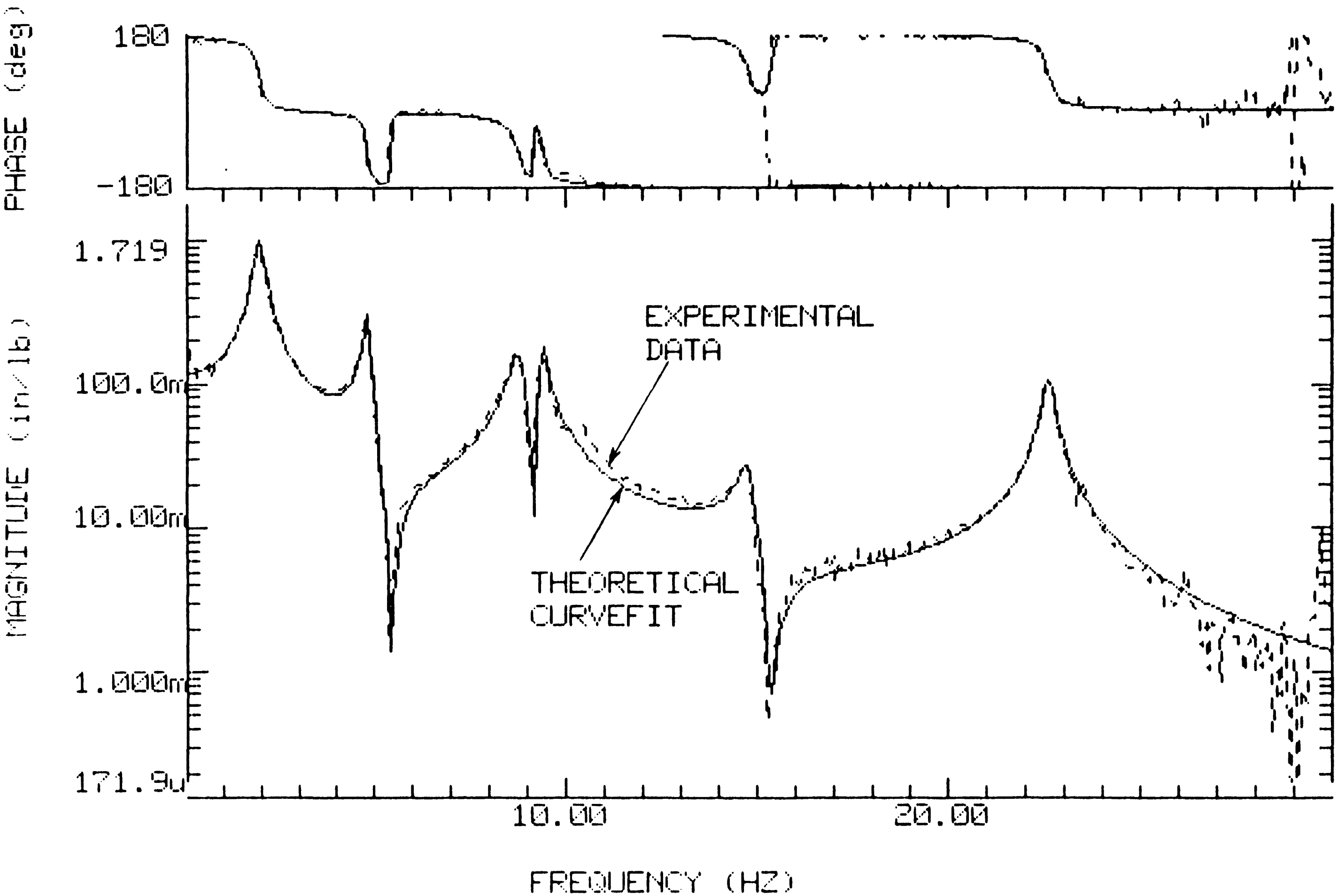

Figure 23: Closed loop displacement FRF uniform gain design. Response at 42 inches from top due to excitation at grid point 9.

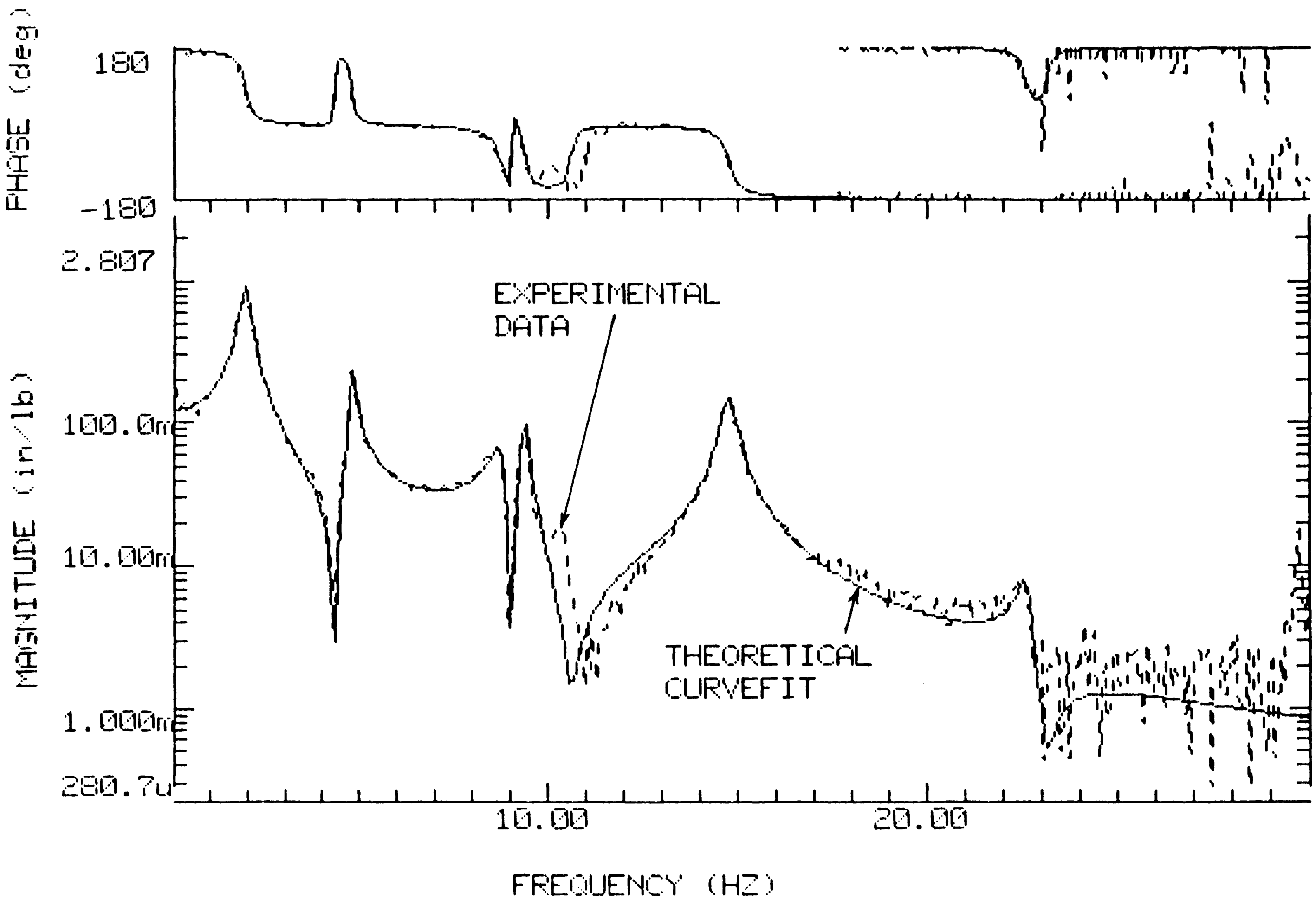

Figure 24: Closed loop displacement FRF uniform gain design. Response at 54 inches from top due to excitation at grid point 9.

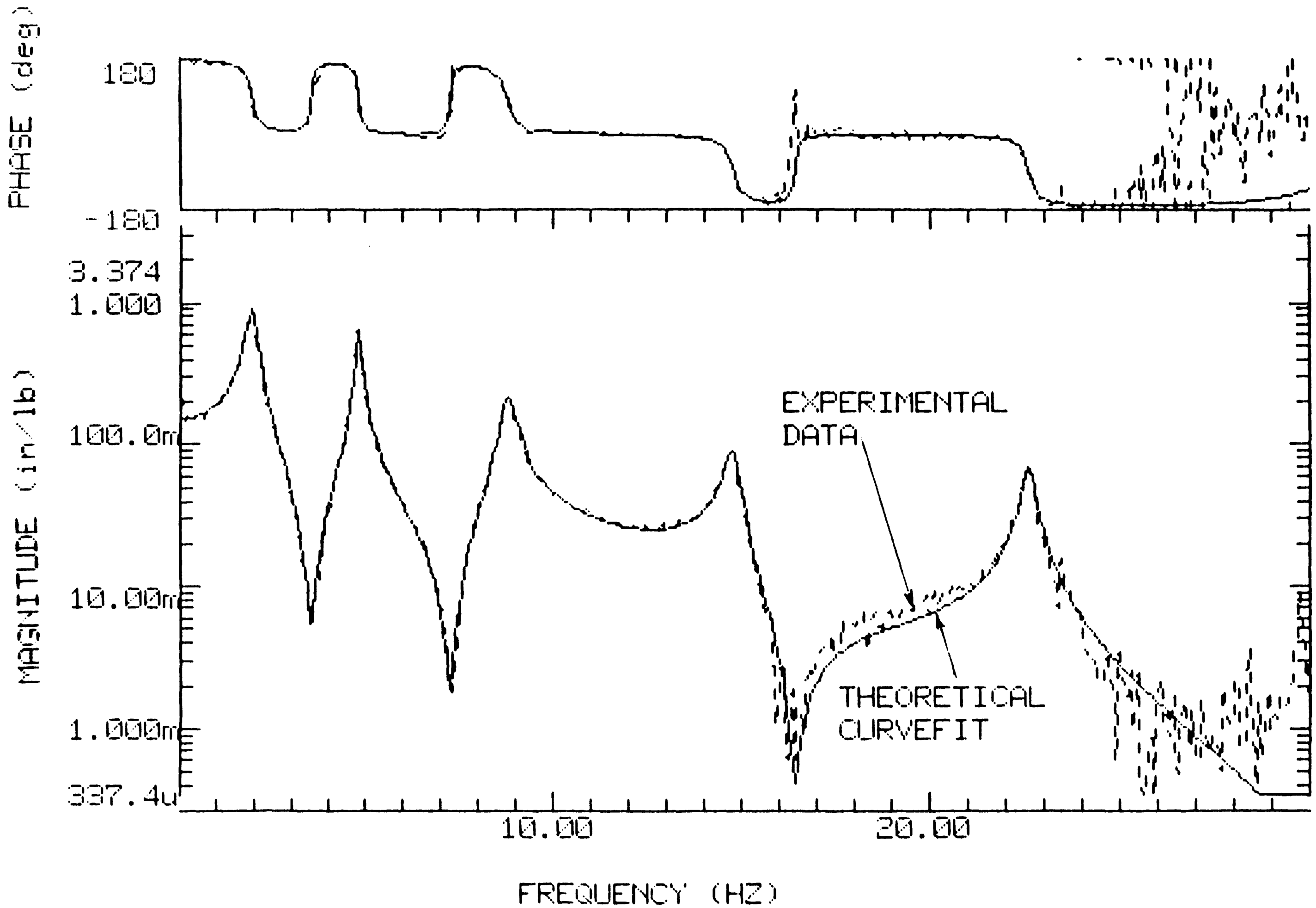

Figure 25: Closed loop displacement FRF uniform gain design. Response at 66 inches from top due to excitation at grid point 9.

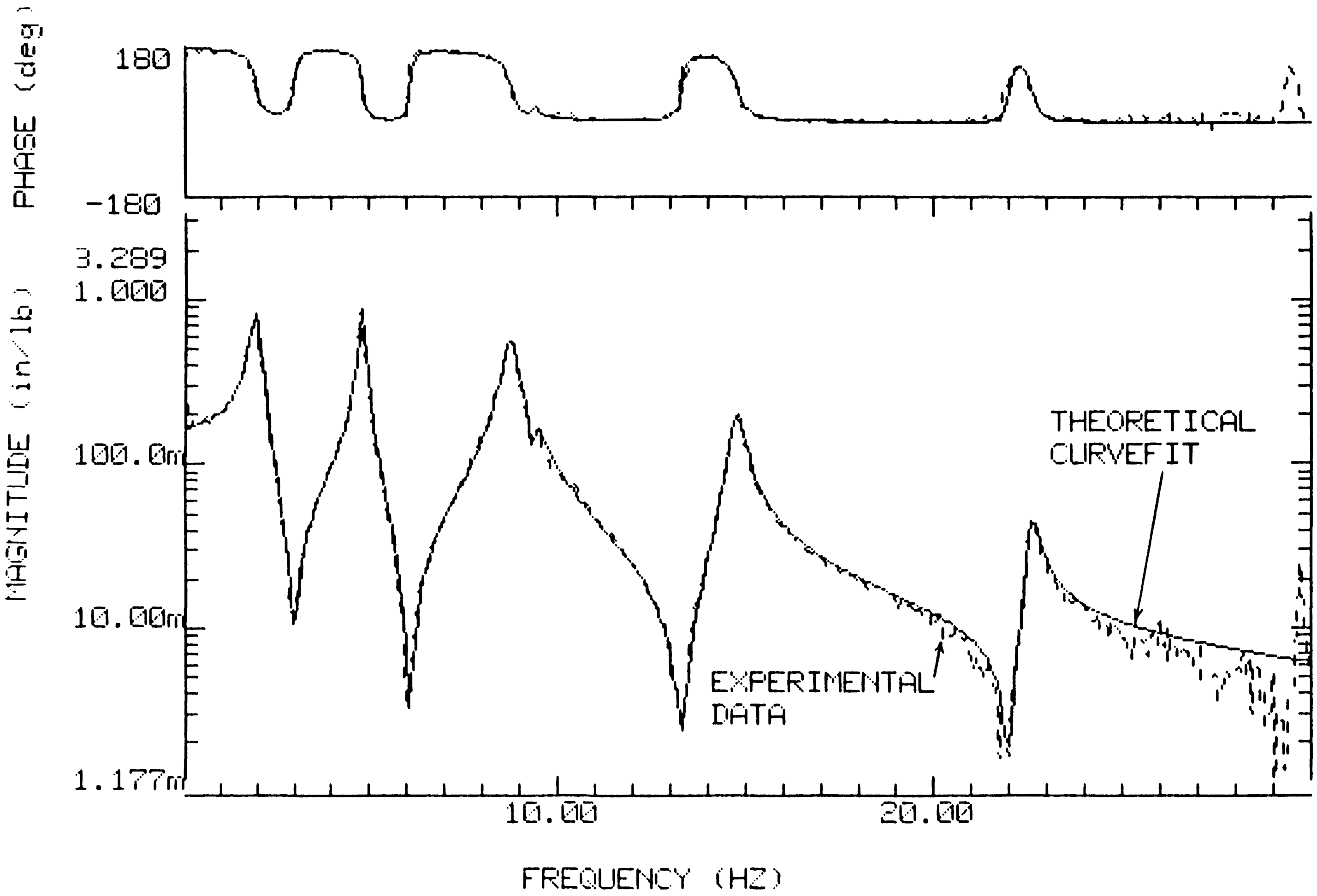

Figure 26: Closed loop displacement FRF uniform gain design. Response at 78 inches from top due to excitation at grid point 9.

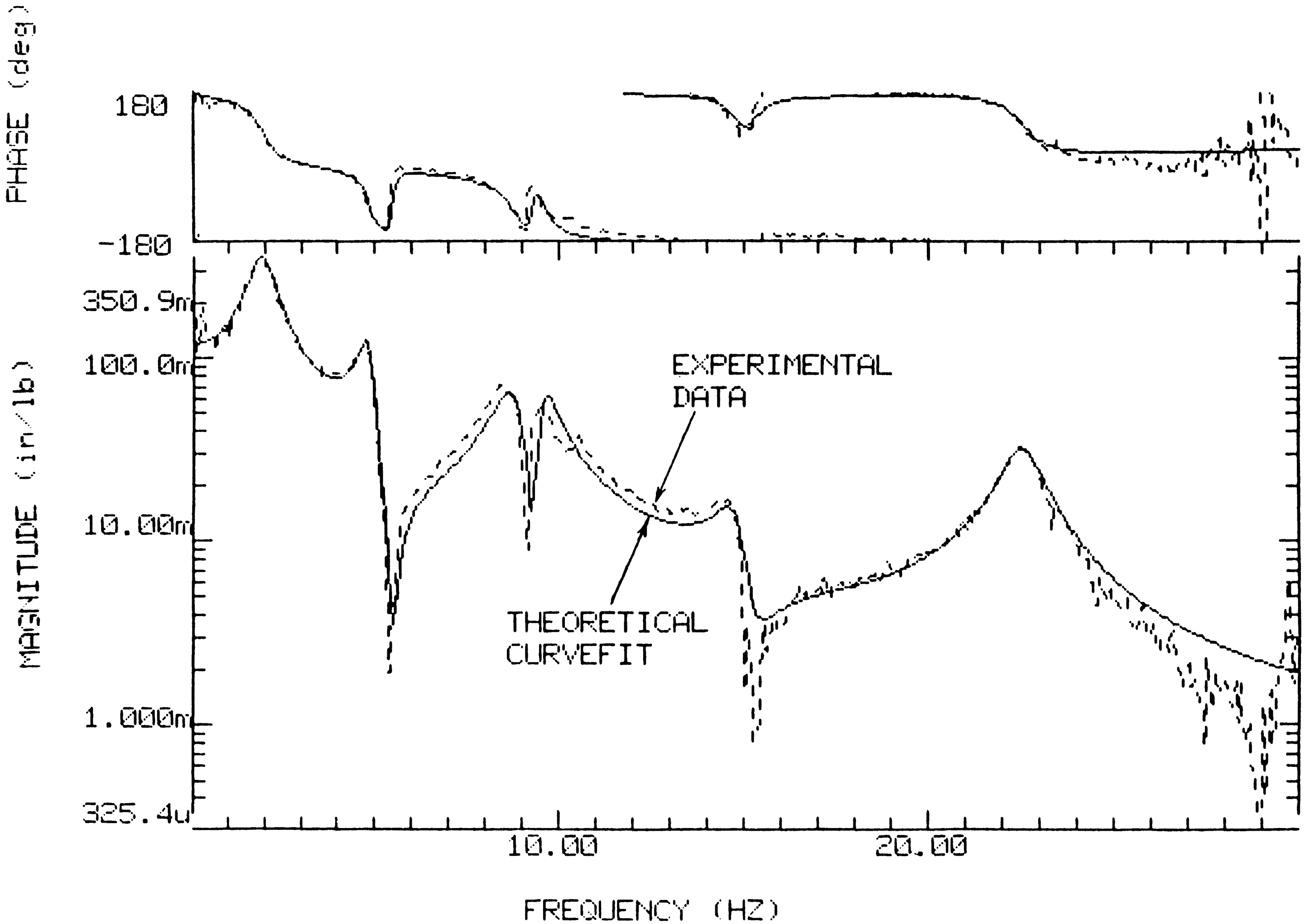

Figure 27: Closed loop displacement FRF optimized gain design. Response at 42 inches from top due to excitation at grid point 9.

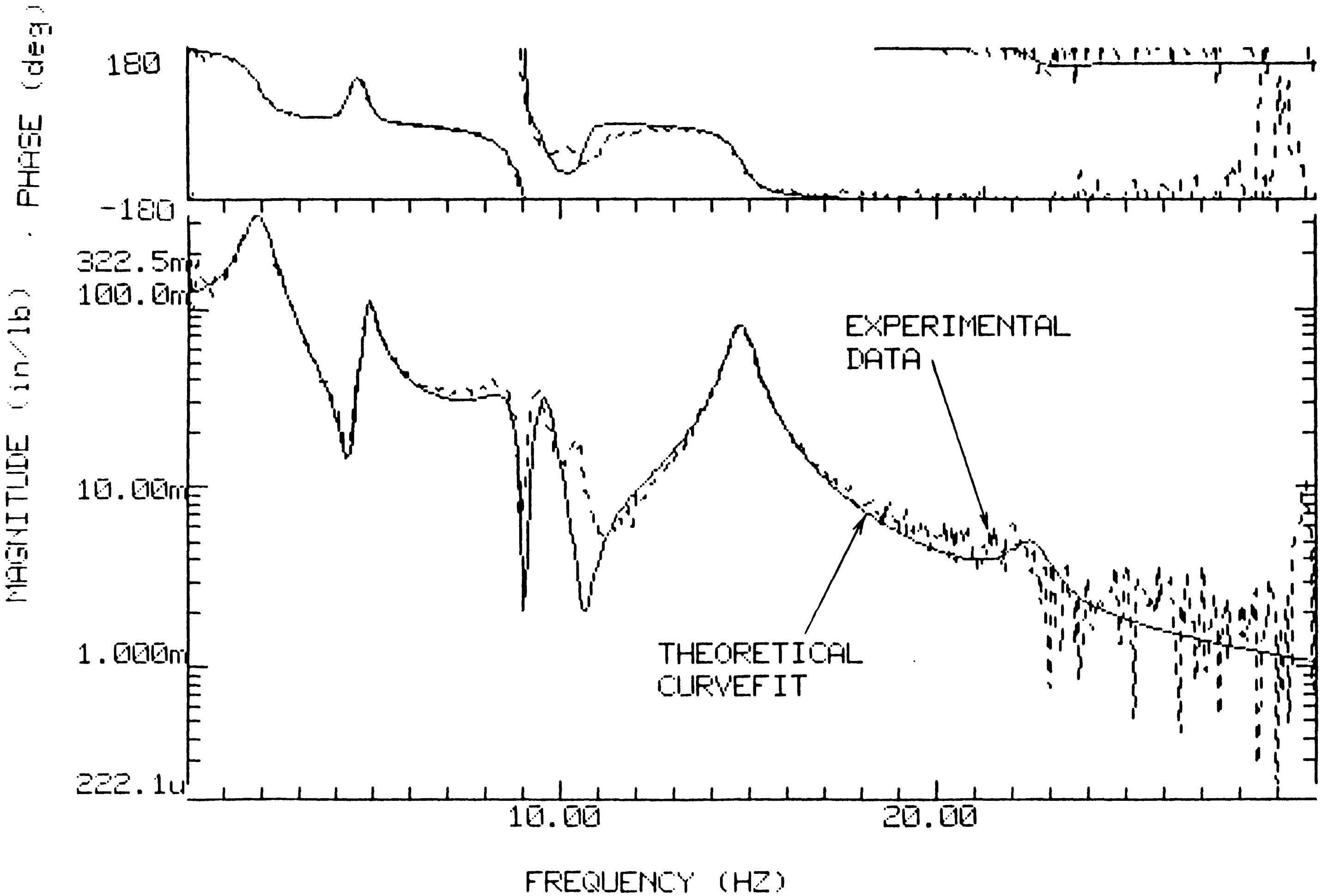

Figure 28: Closed loop displacement FRF optimized gain design. Response at 54 inches from top due to excitation at grid point 9.

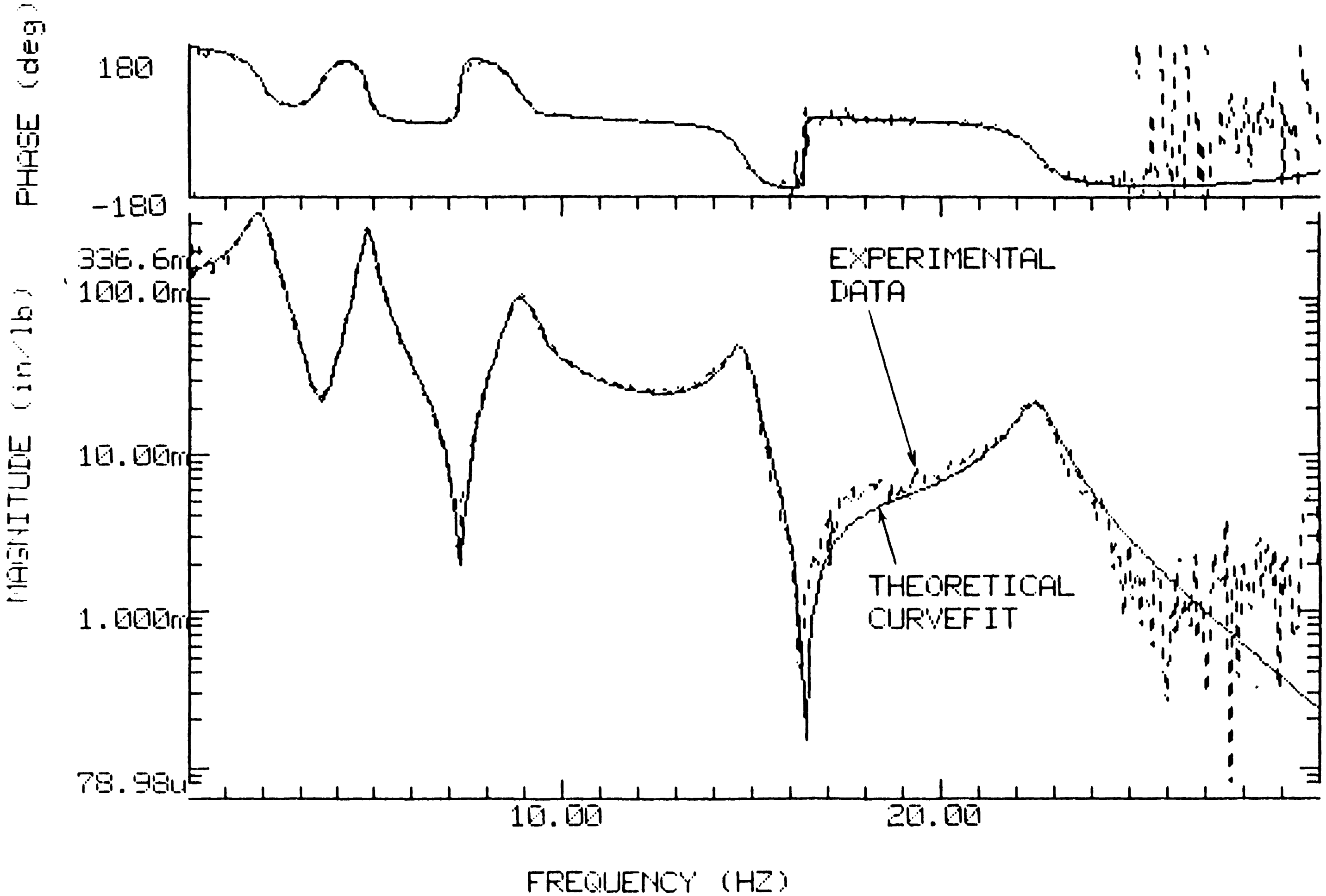

Figure 29: Closed loop displacement FRF optimized gain design. Response at 66 inches from top due to excitation at grid point 9.

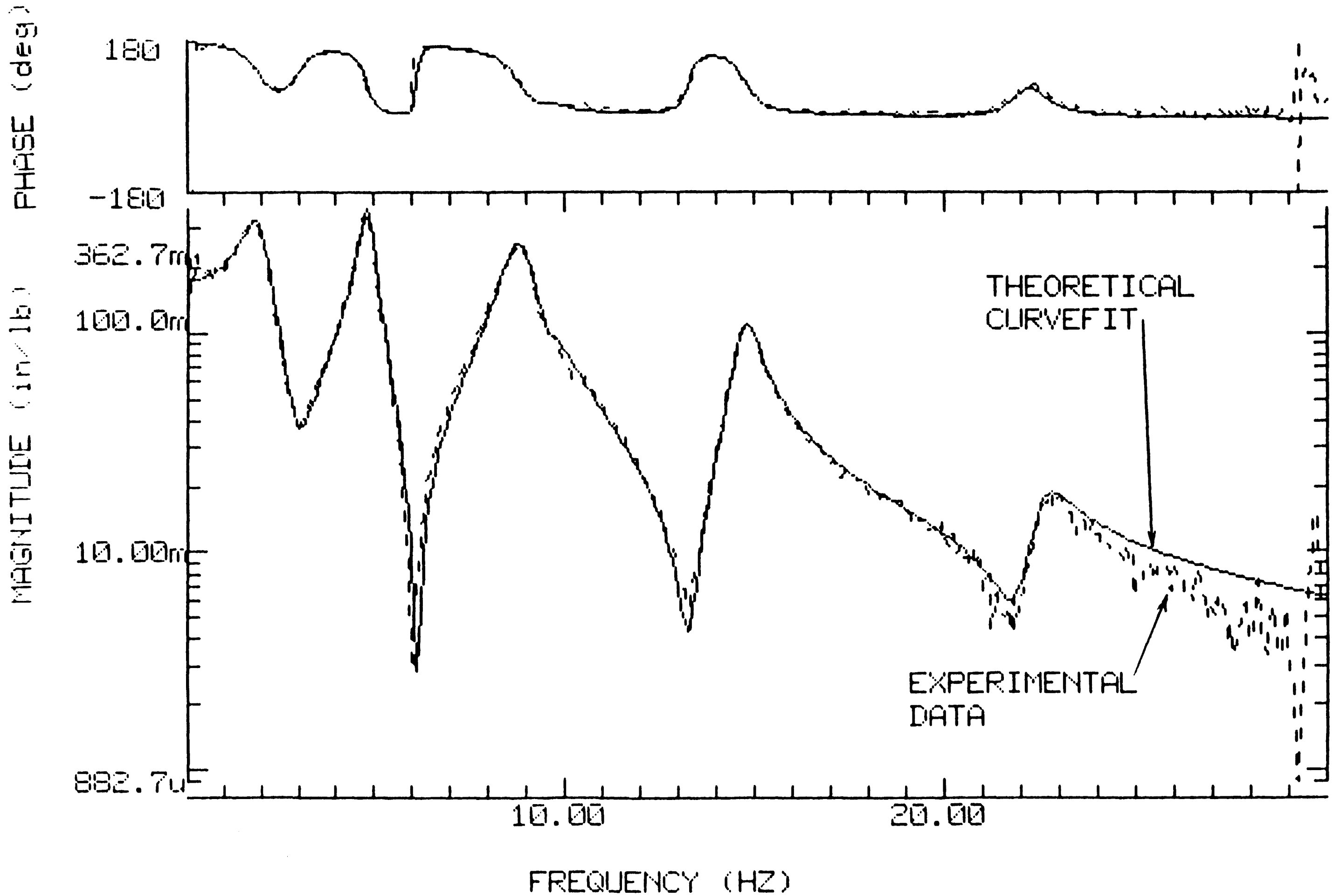

Figure 30: Closed loop displacement FRF optimized gain design. Response at 78 inches from top due to excitation at grid point 9.

Chapter VI

SPATIAL MODAL FILTER

6.1 THEORY

In many control problems, it is necessary to filter a signal in order to get a specific frequency content. A filter is usually either an analog circuit or an analog circuit equation programmed into a digital computer. Unfortunately, this type of filter has its own dynamic response characteristics which may couple with the dynamics of the controlled system and cause instabilities. This problem prompted the investigation of a filter which is based on the characteristics of the system to be controlled. For a structural control problem, this filtering process comes directly from the modal expansion theorem.

The modal filtering problem simply stated is: after sensing the displacement, velocity, or acceleration at points on the structure, now determine the individual modal responses from the measured physical responses. To do this, one must first have a theoretical model of the structure solved for the natural frequencies and mode shapes of the structure. Next, the order of the model is reduced by retaining only the modes which significantly affect the dynamics of the structure. Let N_r = number of retained modes. The number of modes to be sensed must be chosen next, along with the number of sensors to be used and their placement. Let N_s = number of sensors. The order of the model is reduced by retaining in the modal matrix only N_r columns corresponding to the retained modes. The modal matrix is further reduced by retaining only the rows corresponding to the DOFs at which sensors were placed. The modal transformation equation is now:

$$[\Phi]_r \{\eta\} = \{X\} \qquad (6.1)$$

Where $[\eta]$ is the column matrix of the modal responses, $\{X\}$ is the column matrix of the sensed physical responses, and $[\Phi]_r$ is the reduced order modal matrix. If the number of sensors is chosen equal to the number of modes retained ($N_s = N_r$) the reduced order modal matrix will be square and may be inverted to obtain the spatial modal filter:

$$\{\eta\} = [\Phi]_r^{-1} \{X\} \qquad N_s = N_r \qquad (6.2)$$

One can expect the modal responses calculated from Eq. 6.1 to be accurate only if the following conditions are satisfied: 1) the N_r modes retained include all the modes that contribute significantly to the response; 2) the filter matrix $[\Phi]_r^{-1}$ is accurate.

6.2 EXPERIMENTAL APPARATUS AND PROCEDURES

The performance of a spatial modal filter was tested on the beam-cross-cable structure. For this test, six modes were retained and six sensors were used. Bently-Nevada proximity probes were placed at grid points 4, 5, 6, 8, and 9 on the vertical beam and the sixth probe was placed to sense the motion of one of the tip masses on the crosspiece. This corresponds to DOF 19 in the finite element model of the restrained structure. A digital array processor operating at 2000 samples per second was used to perform the matrix multiplication necessary for the filtering. This processor is a Systolic Systems PC-1000 digital array processor. It is programmed from a host IBM Personal Computer. The columns of the filter matrix were each multiplied by the calibration factor of the probe sensing the signal that the entries in that column would multiply. Then the filter matrix was loaded into the PC-1000 by way of the IBM PC. The output signals from the PC-1000 representing the modal displacement signals were then acquired by the STI DAAS. The excitation function generated by the DAAS had the form of an impulse function whose FFT frequency content extended beyond the sixth mode of the structure. Figure 31 is a plot of both the time history of the excitation signal and the amplitude of its FFT. The impulse excitation signal generated by the STI Data Acquisition and Analysis System was put into a power amplifier (Cussons Vibrator Drive Unit) and the power amplifier drove the actuator coil at grid point 9 to excite the structure.

6.3 EXPERIMENTAL RESULTS

Figure 32 presents the FFTs of all six of the physical responses to the assumed impulse excitation. The signal-to-noise ratio of these responses is very poor and it appears as if the higher modes have not been excited to any great degree. The spatial modal filter outputs are presented in Figure 33 FFTs of all six filter outputs are presented. The same excitation function was used to excite the structure for both sets of results presented but the displacement response data was collected during a separate test from the filter response data. Both responses could not be collected in the same test run because 12 channels of data could not be taken due to equipment limitations.

If the filter and all equipment were working properly, each filter output would have only the appropriate single peak, as the filter output for mode 1 has. The results presented in Figure 33 indicate that everything was not working properly; since the filter output for mode 1 is the only output which looks remotely as it should. Even in the filter output for mode 1, the signal-to-noise ratio is much lower than expected. The results presented were not repeatable indicating the presence of mechanical difficulty.

Some factors which may have contributed to the poor quality of the data presented are: 1) there may have been a poor electrical connection from the excitation output of the DAAS to the power amplifier; 2) the power amplifier may have not been generating output consistent with the input impulse excitation; 3) there may have been bad connections between the power unit for the proximity probes and the probes themselves; 4) the numbers for the filter matrix that were placed in the PC-1000 may have been inaccurate; and 5) the signal level input into the DAAS may have been too low. If any of the equipment in use during the test was malfunctioning, that would explain the nonrepeatability of the data. There was insufficient time to completely analyze these problems before the deadline for this report. The problem and a short analysis of the problem is presented here to provide future researchers a base from which to proceed.

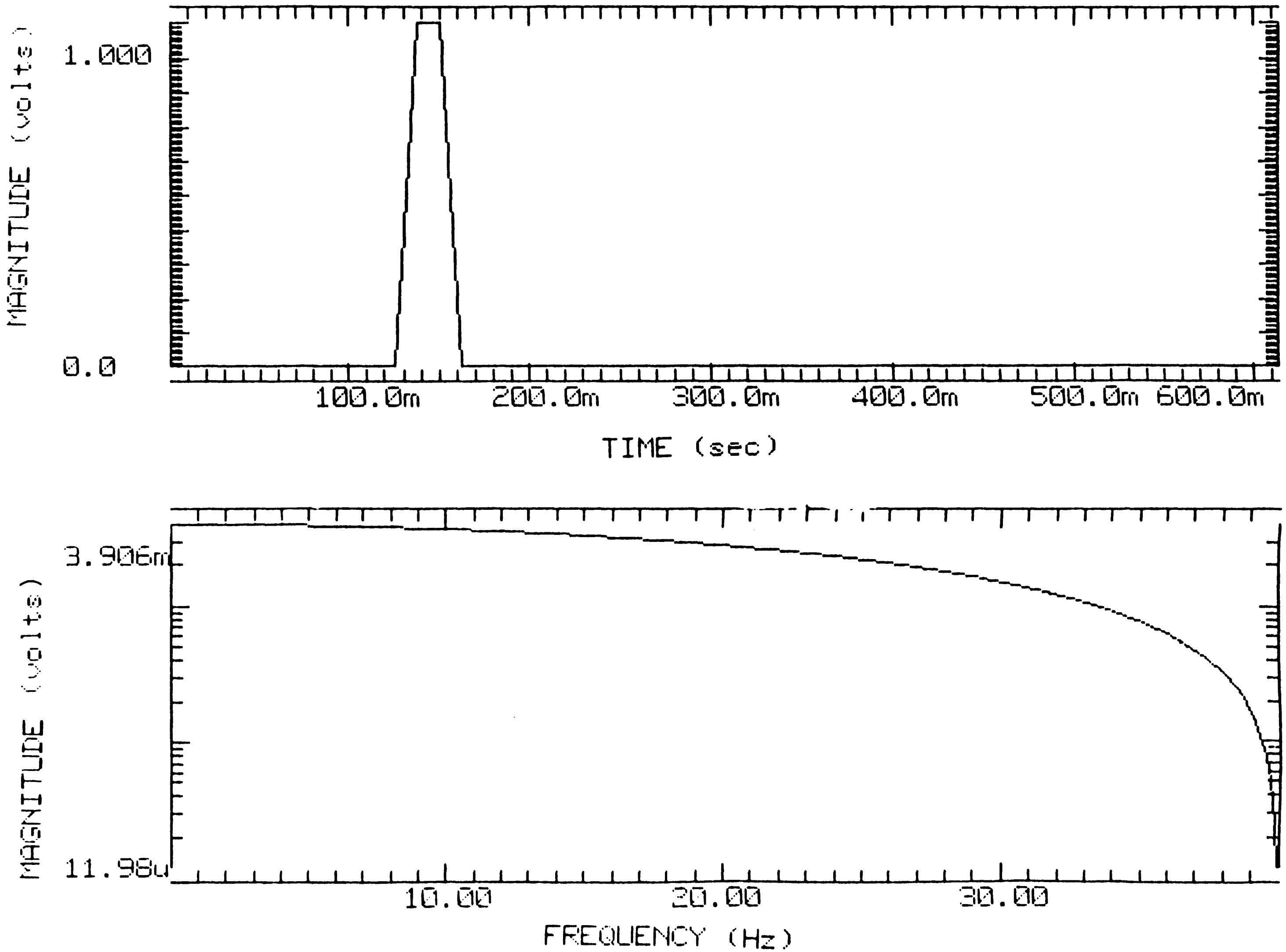

Figure 31: Time history and FFT of the impulse excitation.

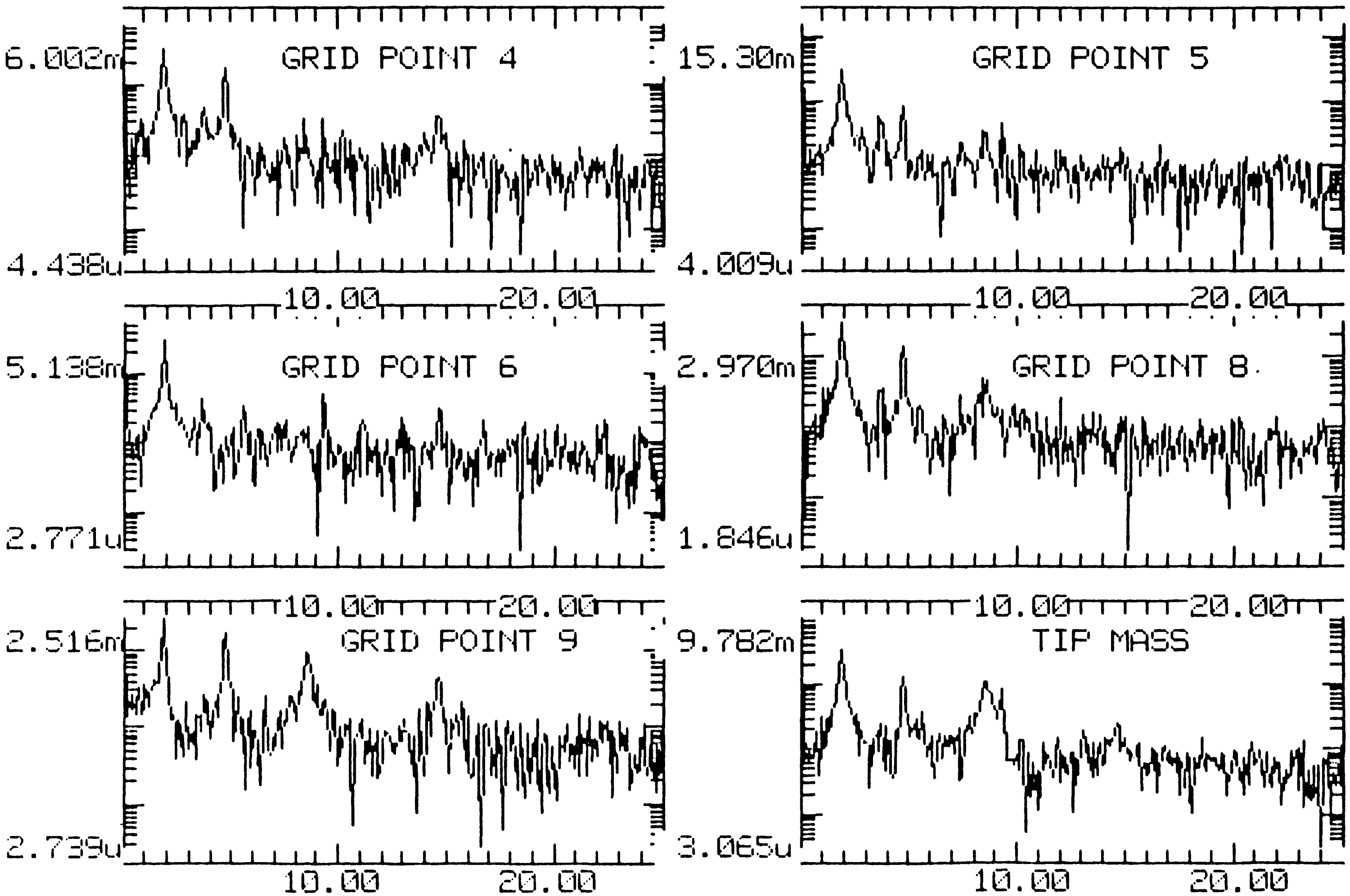

Figure 32: FFTs of displacement responses at grid points 4, 5, 6, 8, 9, and the tipmass to impulse excitation at grid point 9.

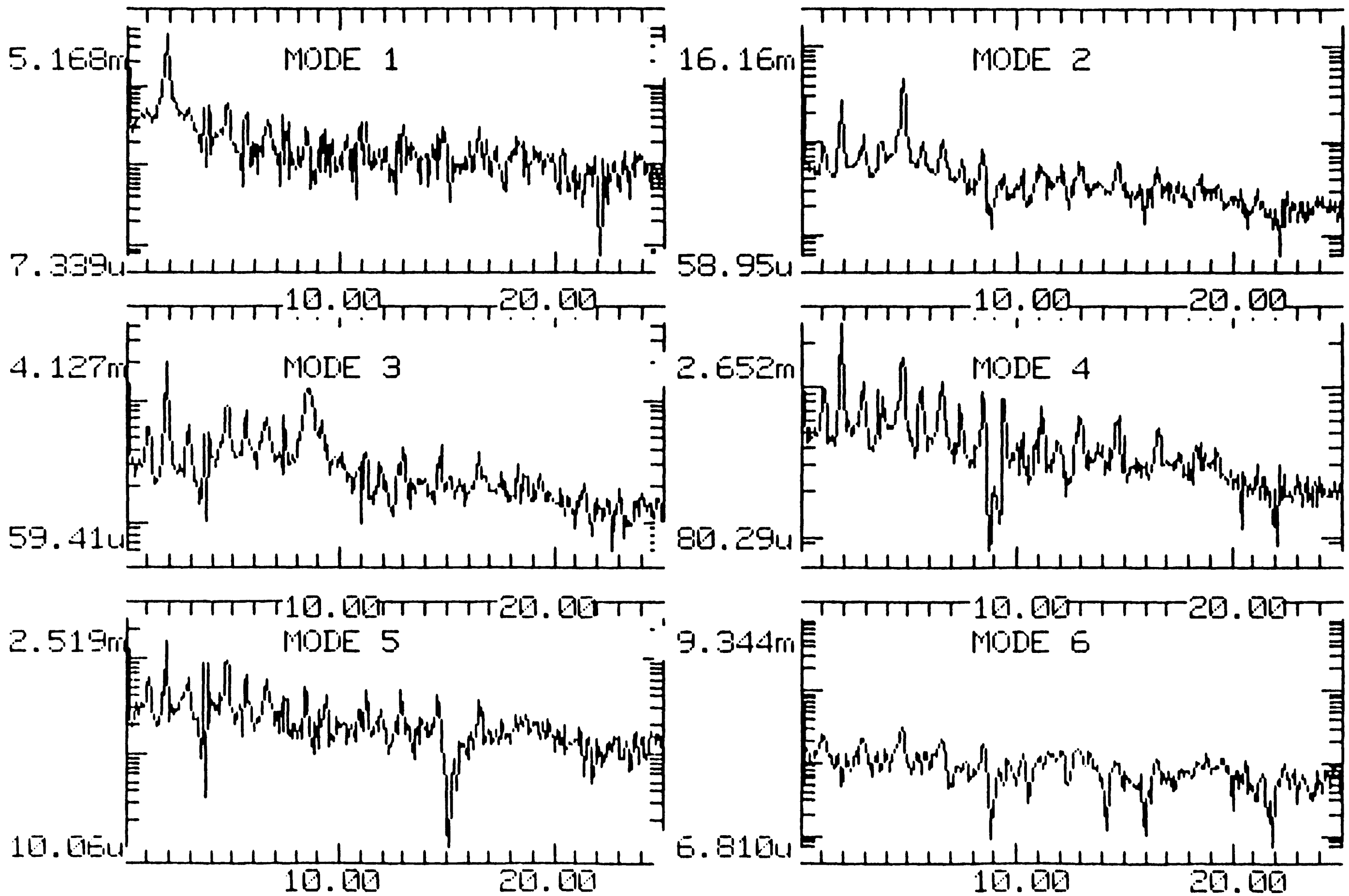

Figure 33: FFTS of spatial modal filter output for modes 1 - 6.

Chapter VII

FINAL REMARKS

With the conclusion of this research, several significant advances have been made in the area of active vibration control. First, a calibration apparatus that yields accurate, repeatable calibration factors for several types of laboratory instruments was designed and produced. Second, a simple laboratory structure was modified to produce a more complex model with a pair of closely-spaced modes making the active control of this modified structure more challenging. A theoretical model for this structure was developed and verified, both in frequency and mode shape, against the laboratory structure. Third, theoretical results in the simultaneous design of structure and control system were verified experimentally, providing a solid base for further theoretical-experimental work in this area. Last, a spatial filter was developed and tested experimentally.

Future work in these areas will involve the simultaneous design of structure-control system with a more complex control system. Also, the spatial modal filter will be investigated in more detail in future work.

REFERENCES

1. Hallauer, W. L. Jr., Skidmore, G. R., and Mesquita, L. C., "Experimental-Theoretical Study of Active Vibration Control," Proc. of 1st International Modal Analysis Conference, Orlando, Florida, Nov. 8-10, 1982.

2. Skidmore, G. R., Hallauer, W. L. Jr., and Gehling, R. N., "Experimental-Theoretical Study of Modal-Space Control," Proc. of 2nd International Modal Analysis Conference, Orlando, Florida, Feb. 6-9, 1984.

3. Skidmore, G. R., "A Study of Modal-Space Control of a Beam-Cable Structure: Experiment and Theory," M. S. thesis, Virginia Polytechnic Institute and State University, May 1983.

4. Masse, M. A., "A Plane Grillage Model for Structural Dynamics Experiments; Design, Theoretical Analysis, and Experimental Testing," M. S. thesis, Virginia Polytechnic Institute and State University, February 1983.

5. Gehling, R. N.,"Experimental and Theoretical Analysis of a Plane Grillage Structure with High Modal Density," M. S. thesis, Virginia Polytechnic Institute and State University, March 1984.

6. Haftka, R. T., Martinovic, Z. N., and Hallauer, W. L. Jr., "Enhanced Vibration Controllability by Minor Structural Modifications," AIAA Paper No. 84-1036-CP, Presented at the AIAA Dynamics Specialists Conference, Palm Springs, California, May 1984. Scheduled for publication in August 1985 issue of AIAA Journal.

7.
Haftka, R. T., Martinovic, Z. N., Hallauer, W. L. Jr., and Schamel, G. C., "Sensitivity of Optimized Control Systems to Minor Structural Modifications," AIAA Paper No. 85-0807-CP, To be presented at the AIAA 26th Structures, Structural Dynamics and Materials Conference, Orlando, Florida, April 1985.

Appendix A

DESIGN OF MAGNETIC FIELD STRUCTURE

A magnetic field structure was designed to produce a radial magnetic field sufficiently strong to be used with a coil as a velocity sensor. The magnetic field structure was designed so that it could be produced out of materials commonly available in a mechanical workshop with the exception of the magnet producing the magnetic field. This magnet had to be relatively small but very strong. A rare earth cobalt magnet sold by Edmund Scientific was chosen for its unusually high strength. This magnet was a 1.00 inch diameter disk 0.375 inches thick which had a residual induction of 8200 gauss. The Edmund Scientific order number is D30,963. The magnetic is placed on a machined base plate made of 1/4 inch thick cold-rolled steel (Figure 34). The contact surface between the magnet and the base plate must be very clean and smooth to insure good conduction of the magnetic field. A capping pole piece also made from cold-rolled steel is now fitted over top of the magnet again making certain of clean, smooth contact surfaces. The pole piece is secured to the base plate through an aluminum bracing collar which is placed over the pole piece and screwed to the base plate with non-magnetic screws. The outer casing made from steel pipe is next fitted to the base plate in the milled grove along the outer edge of the base plate. To complete the magnetic circuit, a top plate is placed over the outer casing fitting the pipe into a milled grove in the top plate. The magnetic circuit generated should be strong enough to hold the field structure together with no other fastenings. The magnetic field structure is now screwed to a 6 by 6 by 1 inch wood base. Figure 2 is a photograph, Figure 34 is line drawing of the assembled magnetic field structure.

The calibration factors for this design of velocity sensor are on the close order of 30 mv/(in/sec). The calibration factors for the other two designs are on the close order of 60 mv/(in/sec) and 180mv/(in/sec) (Ref. 4).

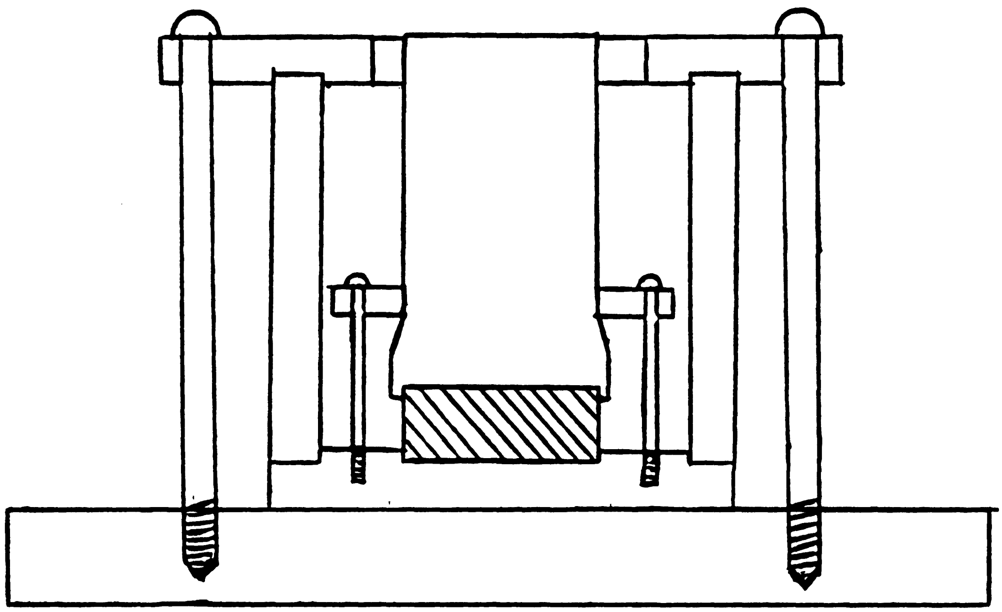

Figure 34: Cross section of assembled magnetic field structure. The magnet is cross-hatched.

Appendix B

RAYLEIGH-RITZ ANALYSIS OF CROSSPIECE

A two degree-of-freedom Rayleigh-Ritz analysis was performed on the complete crosspiece. One DOF was the deflection of the tip mass and the other DOF was the deflection of the center of the beam (Figure 35). The length of the cross piece is 2 L and a mass M is placed at each end. The equation for the deflection of at any point or time on the beam is:

$$v(x,t) = q_1(t)+(q_2(t)-q_1(t))\Psi(x) \qquad \text{(B.1)}$$

where the assumed displacement function is

$$\Psi(x) = 1/2[(x/L)^3-3(x/L)^2+2] \quad 0 \leq x \leq L. \qquad \text{(B.2)}$$

The equation for the potential energy for the entire beam (using symmetry) is

$$V = EI\int_0^L (d^2v/dx^2)^2\,dx. \qquad \text{(B.3)}$$

Integrating the potential energy and presenting the answer in matrix form,

$$V = 1/2[q_1 \;\; q_2]\begin{bmatrix} 6EI/L^3 & -6EI/L^3 \\ -6EI/L^3 & 6EI/L^3 \end{bmatrix}\begin{bmatrix} q_1 \\ q_2 \end{bmatrix} \qquad \text{(B.4)}$$

The 2 by 2 matrix in the equation is the stiffness matrix representing the crosspiece. The equation for the kinetic enerqy of the entire beam (using symmetry) is:

$$T = M\,\dot{q}_2^2 + \rho AL\int_0^L (\dot{v})^2 dx \qquad \text{(B.5)}$$

The integrated kinetic energy equation in matrix form is:

$$T = 1/2[\dot{q}_1 \dot{q}_2]\begin{bmatrix} 34\rho AL/35 & 39\rho AL/140 \\ 39\rho AL/140 & 2M+33\rho AL/70 \end{bmatrix}\begin{bmatrix} \dot{q}_1 \\ \dot{q}_2 \end{bmatrix} \qquad \text{(B.6)}$$

The 2 by 2 matrix is the mass matrix for the crosspiece model.

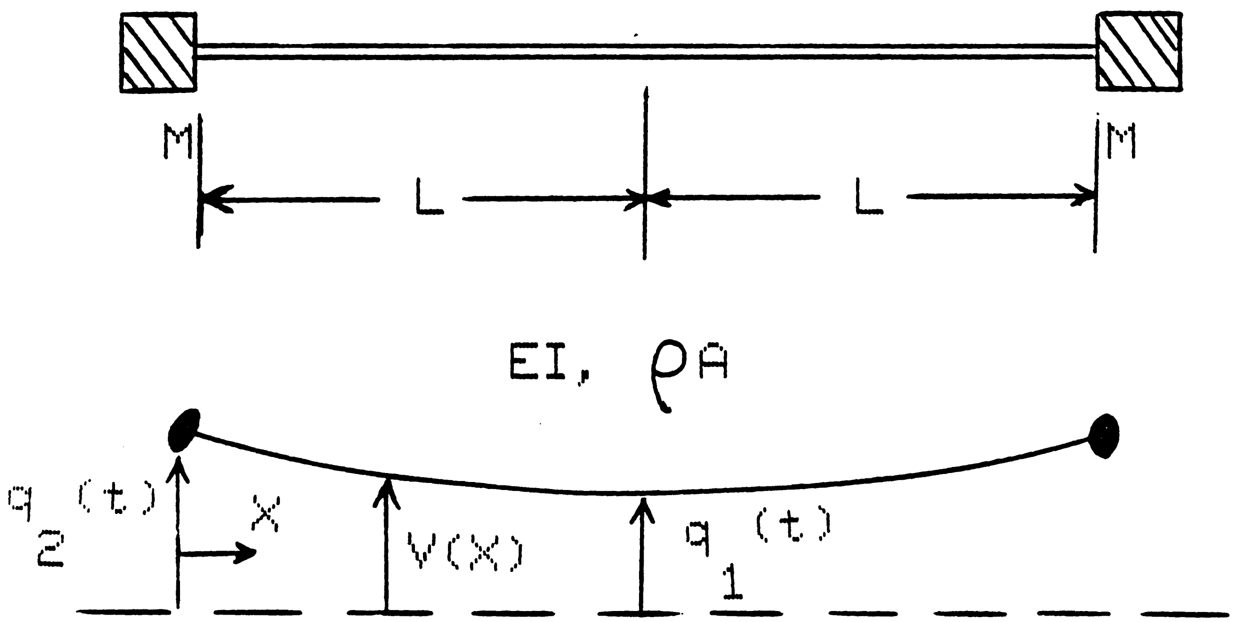

Figure 35: The Rayleigh-Ritz model for the crosspiece.

Appendix C

MAPMODES FINITE ELEMENT MODEL

The finite element model discussed in Chapter III was created using the MAPMODES program. MAPMODES stands for Matrix Algebra Package/Structural MODES. MAPMODES is a special purpose program which contains routines that can generate structural stiffness and mass matrices, perform matrix algebra, and solve the structural eigen-problem for the natural frequencies and mode shapes of the structure. The input file for this program, used to develop the finite element model for the structure and solve for the natural modes is given in Table 6.

Some of the commands in MAPMODES require some additional explanation. The AXFORK command generates the geometric stiffness matrix which accounts for the tension in the vertical beam elements. The first SCALE command sets the tension value at 80.16 pounds. The next set of SCALE commands reduce the tension values in each element to account for the variation in tension along the length of the vertical beam due to gravity loading. BEAMK generates the beam element stiffness matrices for the given beam stiffness and length. The next few lines transform a 9 inch beam element into a 10 inch beam element with a rigid link at either end of the element depending on which transformation matrix is used. BEAMK is also used to generate the element stiffness matrix for the 10 inch beam elements. BEAMM is the MAPMODES command that generates the beam element consistent mass matrices for the structure. The transformation matrices are again used to account for the rigid links. The stiffness arising from the cables in tension was accounted for with the addition of SUBK1 and SUBK2 to the structure stiffness matrix USTIFF. The mass of the cables, cable clamps, three pairs of coils, and the mass of the crosspiece clamp as well as the rotational inertias of the clamp and the crosspiece were modeled by concentrated masses and inertias and added to the structure mass matrix UMASS. The stiffness matrix representing the crosspiece was added with SUBK3 and the mass matrix of the crosspiece was accounted for with the addition of CPIECE1, CPIECE2, and CPIECE3 to UMASS.

The FIXBCS command applied the boundary conditions of zero displacement at the DOFs corresponding to the points of attachment of the cables to the ceiling and floor (unrestrained DOF 1 and 20, respectively). The MODES command was used to solve the eigenvalue problem with the restrained stiffness and mass matrices RSTIFF and RMASS. The solution consisted of the natural frequencies of vibration and the matrix of mode shapes MODAL.

TABLE 6

MAPMODES INPUT FILE

```
START
REMARK                                  5
 CORRECTED BEAM-CABLE ANALYSIS, WITH THREE PAIRS OF
SENSOR/ACTUATOR
 COILS ON BEAM, WITH THE CROSS BEAM ADDED, WITH VARYING TENSION IN
 THE BEAM, WITH A RIGID INSERT AT THE CROSS/BEAM JUNCTION, AND A
 2 DOF RAYLIEGH-RITZ APPROXIMATION FOR THE CROSSPIECE.
 ----- 12 FEBRUARY, 1985
ZERO    USTIFF                         21  21
ZERO    UMASS                          21  21
ZERO    SUBTEN                          4   4
REMARK                                  2
 CREATING THE BASIC GEOMETRIC STIFFNESS MATRIX FOR THE VERTICAL
BEAM

AXFORK  SUBTEN                          1   2   3   4
1.,10.
ADDSM   USTIFF  SUBTEN                  2   2
ADDSM   USTIFF  SUBTEN                  4   4
ADDSM   USTIFF  SUBTEN                  6   6
ADDSM   USTIFF  SUBTEN                  8   8
ADDSM   USTIFF  SUBTEN                 10  10
ADDSM   USTIFF  SUBTEN                 12  12
ADDSM   USTIFF  SUBTEN                 14  14
ADDSM   USTIFF  SUBTEN                 16  16
SCALE   USTIFF                                         80.16
REMARK                                  2
 SCALING THE GEOMETRIC STIFFNESS MATRIX FOR EACH BEAM ELEMENT
 SCALING MADE NECESSARY BY GRAVITY EFFECTS
ZERO    DELTEN                          4   4
AXFORK  DELTEN                          1   2   3   4
1.,10.
SCALE   DELTEN                                         -.694
ADDSM   USTIFF  DELTEN                  4   4
SCALE   DELTEN                                         2.000
ADDSM   USTIFF  DELTEN                  6   6
SCALE   DELTEN                                         1.500
ADDSM   USTIFF  DELTEN                  8   8
SCALE   DELTEN                                         1.408
ADDSM   USTIFF  DELTEN                 10  10
SCALE   DELTEN                                         1.237
ADDSM   USTIFF  DELTEN                 12  12
SCALE   DELTEN                                         1.407
ADDSM   USTIFF  DELTEN                 14  14
SCALE   DELTEN                                         1.136
ADDSM   USTIFF  DELTEN                 16  16
REMARK                                  2
```

```
 CREATING THE TRANSFORMATION MATRICIES TO ACCOUNT FOR THE RIGID
LINKS
 REPRESENTING THE INCREASED STIFFNESS DUE TO THE CLAMP AND
CROSSPIECE
ZERO     RIGID                        4   4
BEAMK    RIGID                        1   2   3   4
9060.,9.0
LOAD     T                            4   4
1.,-1.,0.,0.
0.,1.,0.,0.
0.,0.,1.,0.
0.,0.,0.,1.
LOAD     TO                           4   4
1.,0.,0.,0.
0.,1.,0.,0.
0.,0.,1.,1.
0.,0.,0.,1.
TRANS    T       TT
MULT     TT      RIGID   XX
MULT     XX      T       TRIG
ADDSM    USTIFF  TRIG                14  14
TRANS    TO      TOT
MULT     TOT     RIGID   XX1
MULT     XX1     TO      TRIG1
ADDSM    USTIFF  TRIG1               12  12
REMARK                                2
 ADDING THE BASIC BEAM SITFFNESS MATRIX FOR EACH BEAM ELEMENT
 TO THE STRUCTURE STIFFNESS MATRIX
ZERO     SUBEI                        4   4
BEAMK    SUBEI                        1   2   3   4
9060.,10.0
ADDSM    USTIFF  SUBEI                2   2
ADDSM    USTIFF  SUBEI                4   4
ADDSM    USTIFF  SUBEI                6   6
ADDSM    USTIFF  SUBEI                8   8
ADDSM    USTIFF  SUBEI               10  10
ADDSM    USTIFF  SUBEI               16  16
REMARK                                2
 ACCOUNTING FOR THE RIGID LINKS IN THE MASS MATRIX

ZERO     RMAS                         4   4
BEAMM    RMAS                         1   2   3   4
1.80E-4,9.0
MULT     TOT     RMAS    YY1
MULT     YY1     TO      TRMASS1
ADDSM    UMASS   TRMASS1             12  12
MULT     TT      RMAS    YY
MULT     YY      T       TRMASS
ADDSM    UMASS   TRMASS              14  14
REMARK                                2
 THE FIRST TERM IS THE CLAMP MASS
 THE SECOND TERM IS THE ROTATIONAL INERTIA OF THE CROSSPIECE
```

```
LOADIAG CLAMP                          2
2.470E-03,1.0516E-03
PRINT   CLAMP                          2
THE MASS MATRIX FOR THE CLAMP MASS AND INERTIA PLUS
THE INERTIAS OF THE CROSSPIECE
ADDSM   UMASS   CLAMP                 14  14
REMARK                                 2
 ADDING THE BASIC BEAM ELEMENT MASS MATRIX TO THE STRUCTURE MASS
 MATRIX FOR EACH BEAM ELEMENT
ZERO    SUBMAS                         4   4
BEAMM   SUBMAS                         1   2   3   4
1.80E-4,10.0
ADDSM   UMASS   SUBMAS                 2   2
ADDSM   UMASS   SUBMAS                 4   4
ADDSM   UMASS   SUBMAS                 6   6
ADDSM   UMASS   SUBMAS                 8   8
ADDSM   UMASS   SUBMAS                10  10
ADDSM   UMASS   SUBMAS                16  16
REMARK                                 2
 THE STIFFNESS MATRIX FOR THE UPPER PAIR OF CABLES

LOAD    SUBK1                          2   2
1.,-1.,-1.,1.
SCALE   SUBK1                                      1.191
SCALE   SUBK1                                      2.
ADDSM   USTIFF  SUBK1                  1   1
REMARK                                 2
 THE MASS MATRIX FOR THE UPPER PAIR OF CABLES

LOAD    CABM1                          2   2
0.33333333,0.166666667,0.16666667,0.33333333
SCALE   CABM1                                         2.23E-4
SCALE   CABM1                                      2.
ADDSM   UMASS   CABM1                  1   1
REMARK                                 2
 THE STIFFNESS MATRIX FOR THE LOWER PAIR OF CABLES

LOAD    SUBK2                          3   3
1., 0., -1.,
0., 0., 0.,
-1., 0., 1.
SCALE   SUBK2                                      .8398
SCALE   SUBK2                                      2.
ADDSM   USTIFF  SUBK2                 18  18
REMARK                                 2
 THE MASS MATRIX FOR THE LOWER PAIR OF CABLES

LOAD    CABM2                          3   3
0.33333333,0.,0.16666667,
0., 0., 0.,
```

```
0.16666667, 0.,0.33333333
SCALE   CABM2                                          2.49E-4
SCALE   CABM2                                       2.
ADDSM   UMASS   CABM2                  18  18
REMARK                                  2
 THE CONCENTRATED MASS DUE TO THE CLAMPS ON THE CABLES NEAR THE
 ENDS OF THE BEAM
LOAD    CONCM1                          1   1
3.86E-4
ADDSM   UMASS   CONCM1                  2   2
ADDSM   UMASS   CONCM1                 18  18
REMARK                                  3
 THE STIFFNESS MATRIX FOR THE SPRING REPRESENTING THE CROSSPIECE
  4.7688  X    1.0   -1.0
              -1.0    1.0
LOAD    SUBK3                           1   1
4.7688
ADDSM   USTIFF  SUBK3                  14  14
ADDSM   USTIFF  SUBK3                  21  21
SCALE   SUBK3                                             -1.
ADDSM   USTIFF  SUBK3                  14  21
ADDSM   USTIFF  SUBK3                  21  14
REMARK                                  2
 THE MASS MARITX ELEMENTS DETERMINED BY THE RAYLEIGH-RITZ
APPROXIMATION
 TO THE CROSSPIECE. 2 X 2 SYMMETRIC
LOAD    CPIECE1                         1   1
8.685E-04
LOAD    CPIECE2                         1   1
2.490E-04
LOAD    CPIECE3                         1   1
1.621E-03
PRINT   CPIECE1
PRINT   CPIECE2
PRINT   CPIECE3
ADDSM   UMASS   CPIECE1                14  14
ADDSM   UMASS   CPIECE2                14  21
ADDSM   UMASS   CPIECE2                21  14
ADDSM   UMASS   CPIECE3                21  21
REMARK                                  2
 THE CONCENTRATED MASS DUE TO THE COIL PAIRS MOUNTED ON THE
VERTICAL
 BEAM
LOAD    COILM                           1   1
4.5E-04
ADDSM   UMASS   COILM                  10  10
ADDSM   UMASS   COILM                  14  14
ADDSM   UMASS   COILM                  18  18
FIXBCS  USTIFF  RSTIFF                 19
1,20
FIXBCS  UMASS   RMASS                  19
1,20
```

```
PRINT   RMASS
PRINT   RSTIFF
MODES   RMASS    RSTIFF             11
PRINT   OMEGAS
DUPL    OMEGAS   FREQS
SCALE   FREQS                                     .1591549
PRINT   FREQS
PRINT   GMASS
PRINT   MODAL
STOP
```

Appendix D

BEAM STIFFNESS TESTING

Experimentally determining the stiffness of a beam section proved to be relatively easy, once the proper equipment was set up. Two tables were set so that their edges were about six inches apart and a multipurpose loading device was placed across the opening (Figure 36). The beam section to be tested was then placed on two simple supports in the loading device. A dial gauge was placed on top of the loading device with its sting projecting through a hole in the top of the loading device and touching the top of the beam section. The dial gauge was set to zero with the beam section in this free condition. Several measured weights were hung from the beam section and the deflection due to each recorded.

A linear regression was performed on the data to obtain the slope of the line in pounds per inch. Figure 37 is a plot of the data obtained for the testing of the aluminum beam section from the crosspiece. The distance between the simple supports was measured along with location of the loading and the location of the dial gauge sting. The bending stiffness of the beam section could then be determined from the equation for the deflection of a simply supported beam subjected to a load.

The steel beam section tested was a piece of the original beam from which the vertical beam in the beam-cross-cable was cut. Also, the aluminum beam section was a piece of the original beam from which the crosspiece was constructed. The EI value determined for the steel beam section was 9060 $lb\text{-}in^2$ and the EI of the aluminum beam section was found to be 2681 $lb\text{-}in^2$.

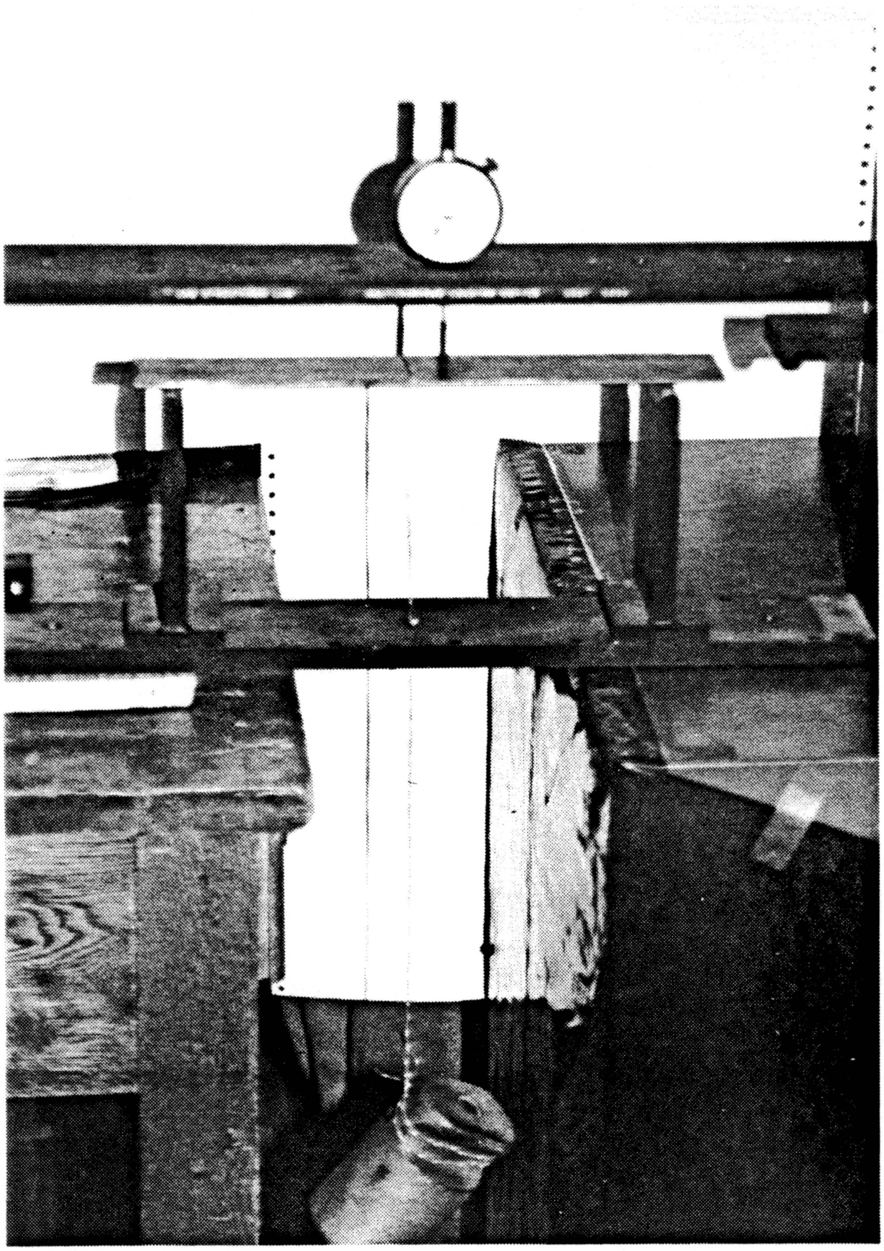

Figure 36: Photograph of beam stiffness testing setup. Note weight hanging from beam section.

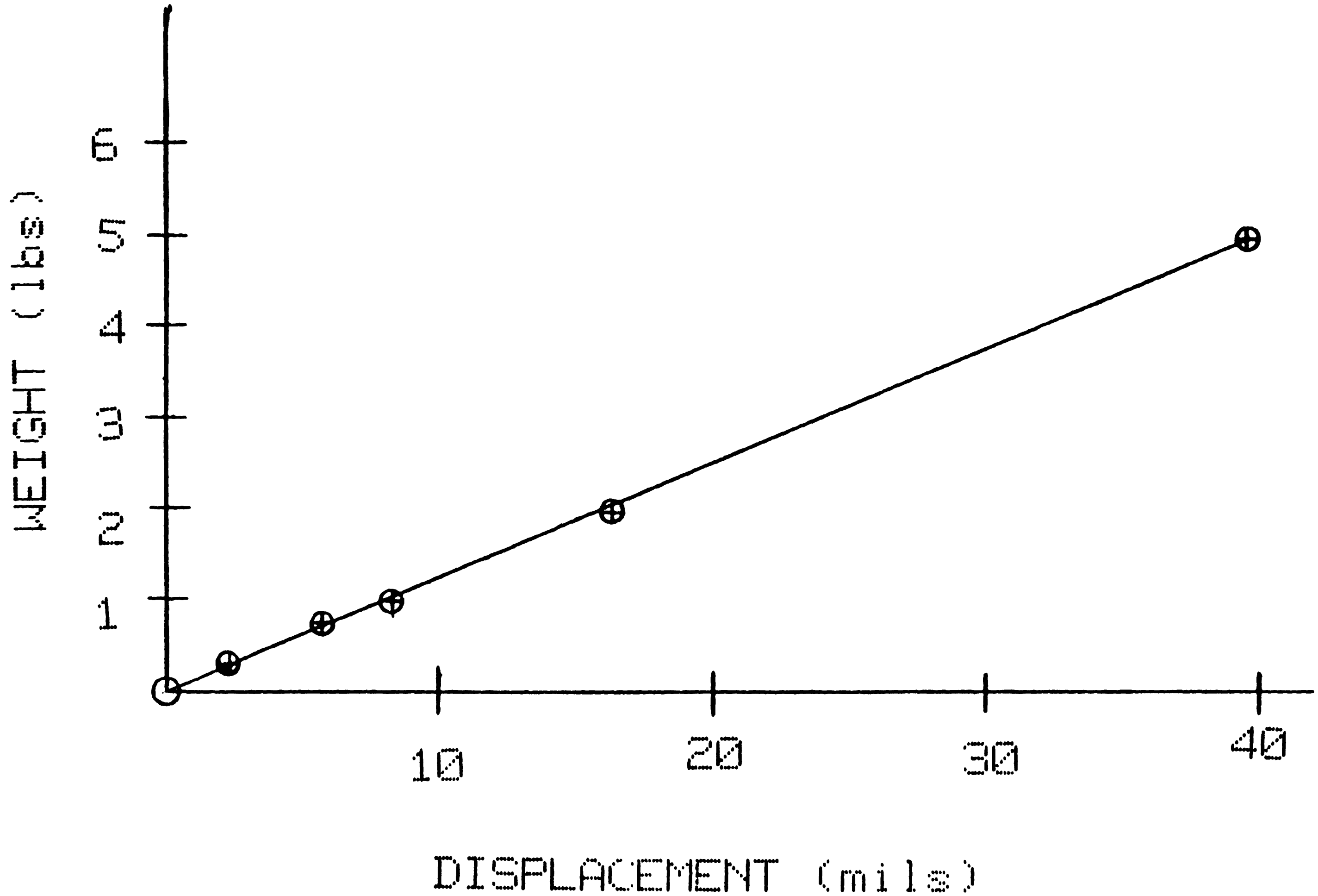

Figure 37: Plot of data points from testing of aluminum beam section. Note the linearity of the data.

The vita has been removed from the scanned document